12-7-2017

Development of an algorithm for satellite remote sensing of sea and lake ice

Peter Dorofy
Rowan University

DEVELOPMENT OF AN ALGORITHM FOR SATELLITE REMOTE SENSING OF SEA AND LAKE ICE

by

Peter T. Dorofy

A Thesis

Submitted to the
Department of Civil and Environmental Engineering
College of Engineering
In partial fulfillment of the requirement
For the degree of
Master of Science in Civil Engineering
at
Rowan University
November 17, 2017

Thesis Chair: Rouzbeh Nazari, Ph.D.

Acknowledgments

This work was funded by Rowan University and the National Oceanic and Atmospheric Administration (NOAA). The views, opinions, and findings contained in this report are those of the author and should not be construed as an official National Oceanic and Atmospheric Administration or U.S. Government position, policy, or decision. I wish to express my gratitude to Peter Romanov at NOAA Cooperative Remote Sensing Science and Technology Center (CREST) and Jeffrey Key at NOAA, both of whom provided scientific advisement and editing for content. In addition, I like to thank my Advisor, Professor Rouzbeh Nazari, for research guidance and editing for content as well as the undergraduate students at Rowan University: Matthew Grosmick, Godfrey Joyner, and Andrew Plucinsky for assisting with data collection.

Abstract

Peter Dorofy
DEVELOPMENT OF AN ALGORITHM FOR SATELLITE REMOTE SENSING OF SEA AND LAKE ICE

2017-2018
Rouzbeh Nazari, Ph.D.
Master of Science in Civil Engineering

Satellite remote sensing of snow and ice has a long history. The traditional method for many snow and ice detection algorithms has been the use of the Normalized Difference Snow Index (NDSI). This manuscript is composed of two parts. Chapter 1, *Development of a Mid-Infrared Sea and Lake Ice Index (MISI) using the GOES Imager*, discusses the desirability, development, and implementation of alternative index for an ice detection algorithm, application of the algorithm to the detection of lake ice, and qualitative validation against other ice mapping products; such as, the Ice Mapping System (IMS). Chapter 2, *Application of Dynamic Threshold in a Lake Ice Detection Algorithm*, continues with a discussion of the development of a method that considers the variable viewing and illumination geometry of observations throughout the day. The method is an alternative to Bidirectional Reflectance Distribution Function (BRDF) models. Evaluation of the performance of the algorithm is introduced by aggregating

classified pixels within geometrical boundaries designated by IMS and obtaining sensitivity and specificity statistical measures.

Table of Contents

Table of Contents (Continued)

List of Figures

List of Tables

Chapter 1

Development of a Mid-Infrared Sea and Lake Ice Index (MISI) Using the GOES Imager

Abstract

An automated ice-mapping algorithm has been developed and evaluated using data from the GOES-13 imager. The approach includes cloud-free image compositing as well as image classification using spectral criteria. The algorithm uses an alternative snow index to the Normalized Difference Snow Index (NDSI). The GOES-13 imager does not have a 1.6 μm band, a requirement for NDSI; however, the newly proposed Mid-Infrared Sea and Lake Ice Index (MISI) incorporates the reflective component of the 3.9 μm or mid-infrared (MIR) band, which the GOES-13 imager does operate. Incorporating MISI into a sea or lake ice mapping algorithm allows for mapping of thin or broken ice with no snow cover (nilas, frazil ice) and thicker ice with snow cover to a degree of confidence that is comparable to other ice mapping products. The proposed index has been applied over the Great Lakes region and qualitatively compared to the Interactive Multi-sensor Snow and Ice Mapping System (IMS), the National Ice Center ice concentration maps and MODIS snow cover products. The application of MISI may open additional possibilities in climate research using historical GOES imagery. Furthermore, MISI may be used in addition to the current NDSI

in ice identification to build more robust ice mapping algorithms for the next generation GOES satellites.

Introduction

Types of lake and sea ice. Sea and lake ice exhibits a variety of forms based on age and growth conditions. Frazil ice forms when water first begins to freeze. These crystals typically have diameters of 3 to 4 mm and may float and bond together to form thin sheets of ice that are called nilas. Initially, nilas is dark, but becomes lighter as it thickens. Over time, the ice continues to thicken and eventually becomes stable, forming a smooth bottom. This type of ice is called congelation ice [1].

Sea ice and lake ice differ in several ways. Lake ice forms from fresh water or snow, containing minimal pockets of brine. Whereas brine found in sea ice contributes to scattering, in fresh water ice, air bubbles are the primary scatterers of light. Lake ice also tends to be smooth, forming in a gentler environment; unlike sea ice, which forms into various shapes due to the turbulent conditions of ocean water.

Reflectance of snow and ice. Spectral properties vary within different forms of ice. Within the visible (about 0.4–0.7 μm; hereafter "VIS"), fresh snow

may have a reflectivity greater than 0.9, whereas congelation ice has a reflectivity closer to 0.6. The reflectivity of refreezing ice is even lower, around 0.5 [2].

Further down the spectrum in the MIR, there is an apparent reversal in the reflectance of snow and thin ice. A study in the measurement of directional hemispherical reflectance spectra of frost, snow, and thin ice was conducted [3]. The study revealed that the there is an increase in the reflection of thin ice (0.4 cm) over snow beyond 3 μm. In addition, ice has a surface scattering peak near 3.2 μm. The study also revealed that as grain size decreases; for example, from fine snow to frost, the grains become optically thin allowing an increase in volume scattering. The result is additional peaks in reflectance such as frost near 3.7 μm [3]. This particular laboratory study may be indicative that the MIR reflectance of gray ice with a thickness 0.4 cm, is higher (>2%) than various snow types (disaggregated granular, fine acicular) with an MIR that is relatively lower reflectance (<2%).

There is a variation of snow reflectance that is dependent on grain size. Snow reflectance decreases as grain size increases. As snow ages grain size increases, contributing to a drop in reflectance. This difference in reflectance is significant in the shortwave infrared (SWIR), particularly at approximately 1.6 and 2.2 μm). Above 3 μm there are similar spectral signatures of snow larger than 50 μm; however, there is a significant peak in reflectance for 10 μm grain

size near 4 μm. In addition, ice has surface scattering effects near 3.2 μm [3]. In the case of lake ice, air bubbles are the primary contributors to scattering and the resulting reflectance. As ice melts, air bubbles become filled with water, resulting in a decrease in reflectance [4].

Laboratory observations reveal that reflectance of ice increases with thickness [5,6]. The reflectance at wavelengths between 0.5 and 1 μm is relatively uniform for an ice thickness less than 5 cm. However, there is a rapid increase in reflectance for thicknesses greater than 5 cm. The increase becomes more asymptotic as the ice continues to grow in thickness. With increasing wavelength there is greater absorption. Beyond a thickness of 17 cm, reflectance continues to rise significantly in the visible between 0.4 μm and 0.6 μm. The asymptotic rise continues for wavelengths of 0.7 μm and greater. Backscattering effects contribute to the increase in reflectance. As ice thickens there is more opportunity for backscattering. As pointed out earlier, snow reflectance is generally large, near 0.9, due to the large scattering coefficients for snow in the visible [4]. In the classification method for this paper, bare thick ice and snow-covered ice are treated the same as they both appear to have high reflectance.

Ice reflectance substantially increases when ice thickness is above 5 cm. In this paper, this is used for differentiating between two ice categories, thin/broken ice with less than 5 cm thickness (gray ice, nilas, frazil ice) and thick ice,

potentially snow covered, with thicknesses of above 5 cm. With a high ratio of reflectance in the VIS to MIR of thick ice and a relatively smaller ratio of reflectance in the VIS to MIR of thinner ice or nilas, these observed ratio differences may help to delineate thick ice and nilas.

Satellite remote sensing of snow and ice. Land, water, thin ice, and thin clouds generally have low reflectance in the visible; whereas, snow, thick ice, and thick clouds have relatively high reflectance in the visible. The properties of ice, or, more specifically "thick ice", resemble the optical properties of snow. Discriminating between features with extreme differences in reflectance is relatively easy. The difficulty arises when the reflectance is similar. For example, distinguishing thick ice from thick clouds that have similarly high reflectance can be very challenging. Discriminating between open water and nilas may also be problematic as they have similar low reflectance. Discriminating between ice and clouds in satellite imagery has a long history in development. Earth orbiting remote sensing data for snow reflectance investigation began with Skylab's Earth Resources Experiment Package (EREP) S192 multispectral scanner which began service in 1973. This instrument operated in various bands including VIS-SWIR (0.41–2.34 μm), and longwave infrared (10.07–12.68 μm). By using the ratio of very near infrared (VNIR) channels to near infrared (NIR) or SWIR, snow can be discriminated from clouds [7]. Furthermore, using the ratio of the 1.6–0.754 μm,

clouds can be distinguished from snow [8]. The normalized difference of Landsat's Thematic Mapper TM bands (0.52–0.60 μm) and (1.55–1.75 μm) can be used for automated snow mapping [9].

The Normalized Difference Snow Index (NDSI) serves as the basis for the Moderate Resolution Imaging Spectroradiometer (MODIS) snow-mapping product [10]. NDSI, which has been used for snow mapping applications [11], is the normalized difference between the 0.6 μm visible band and the 1.6 μm SWIR band. In the event of a sensor failure the 2.1 μm band may be used in place of the 1.6 μm band [12]. There have been other variations to NDSI; in addition to visible and NIR channels, other channels have been investigated in cloud/snow discrimination. For example, an alternative to the VIS-SWIR normalized ratio for NDSI is the visible-thermal infrared (VIS-TIR) normalized ratio called normalized difference thermal snow index, NDTSI, [13].

One of the channels of particular interest is the MIR band near 3.9 μm. The NOAA Advanced Very High Resolution Radiometer (AVHRR) first operated onboard TIROS-N in 1978. Subsequent NOAA polar orbiting satellites also carried the AVHRR, though there have been three versions of the instruments with some differences in the channels. Channel 3 of the AVHRR instrument operates in 3.55–3.93 μm range, which has been used extensively for snow/cloud discrimination. The radiance measured in this wavelength range is comprised of

both reflected solar and emitted thermal components. A method for extracting the reflected component has been demonstrated [14]. The method uses the channel 4 temperature to estimate and remove the thermal component of channel 3. This has proved useful and showed promise for snow/cloud discrimination [15]. The snow/cloud discrimination at 3.7 or 3.9 microns refers to liquid clouds rather than ice clouds, as ice clouds will have relatively low reflectance at MIR wavelengths, similar to snow or ice. The basis of using the 3.7 μm reflectance was employed in snow/cloud discrimination from the ratio of visible to MIR, coined as the Snow Index (SI) used for automating snow mapping [16]. In another study, the 0.675 μm channel and the reflective component of 3.75 μm channels of MTSAT-1R satellite were used for snow/cloud discrimination along with a split window method for sea surface temperature (SST) for sea ice detection [17].

The focus of this paper is to apply the Snow Index [16] to lake ice mapping. Whereas a goal of the SI was to distinguish snow pixels from snow-free land, a goal of MISI is to distinguish between lake ice pixels and ice-free pixels. Furthermore, MISI considers the spectral property differences between thick ice and the relatively darker, gray ice; such as frazil or nilas in both the VIS and the MIR.

Data and Methods

Study area and data acquisition. Our study area is the Great Lakes, which are located in the northeastern Midwest United States along the U.S.–Canadian border. The Great Lakes are the largest supply of freshwater in the world. About 18% of the world's freshwater supply provides drinking water to approximately 40 million U.S. and Canadian citizens. The lakes cover a combined area over 94,000 square miles and have a combined volume of 5500 cubic miles.

Ice on the Great Lakes region (Figure 1) impacts society in various sectors, including hydropower generation, commercial shipping, the fishing industry, and recreation. Ice cover in the Great Lakes can vary significantly from year to year. Studying ice coverage over the Great Lakes provides an opportunity for scientists to study regional climate patterns.

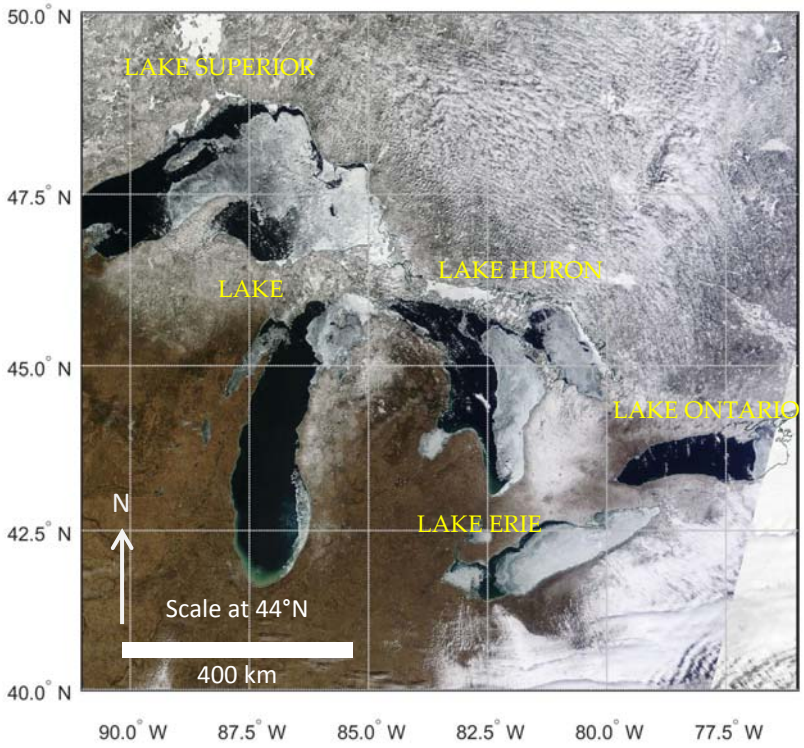

Figure 1. Ice cover on the Great Lakes. Image acquired on 17 March 2015 (NASA).

The U.S. National Oceanic and Atmospheric Administration's (NOAA) Geostationary Operational Environmental Satellite (GOES) series has been the backbone of geosynchronous environmental monitoring of the Americas since 1975. These satellites provide both the temporal resolution and regional coverage over the Great Lakes required for this study.

Matlab (R2015A) is used for developing the algorithm. Some of the core code can be found in appendix B. Data collected by the GOES-13 imager instrument is being used in this study. The GOES imager is a five-channel instrument (one visible, four infrared), as listed in Table 1.

Table 1

GOES-13 imager channels.

GOES-13 Imager					
Channel #	1 (VIS)	2 (MIR)	3 (Moisture)	4 (IR1)	6 (IR2)
Wavelength Range (μm)	0.54–0.71	3.73–4.08	5.90–7.28	10.19–11.18	13.00–13.71
Central Wavelength (μm)	0.62	3.90	6.54	10.7	13.34
Instantaneous Field of View (IFOV), km	1	4	4	4	4

All channels except channel 3 are used in this study. GOES imagery is obtained from the NOAA Comprehensive Large Array-data Stewardship System (CLASS). The GOES imager GVAR (GOES Variable Format) sensor counts are stored as 10-bit. The data is downloaded as a netCDF file. The original 10-bit data were converted to 16-bit to be stored as netCDF (netCDF data is stored as 16-bit). A conversion is therefore made from 16-bit back to the original 10-bit. Data from channels 2 through 6 were resized to 1 km resolution to fit the spatial resolution of channel 1 data. Bicubic interpolation was applied in the transformation. Counts were converted to radiance using the calibration procedure provided by NOAA's Office of Satellite and Product Operations (OSPO).

In order to build a robust ice classification model, it is vital that frequent observations are made throughout the day; thereby increasing the chance of obtaining cloud-free pixels. A daily composite image with significant reduction in cloud contamination can then be built. Data acquisition times are every half-hour from 1600 UTC to 2030 UTC. These are the times that GOES-13 is in the

continental US (CONUS) extended scan mode with the exclusion of near 18:00 UTC which is during the time GOES-13 is operating in full disc mode. These times also correspond to daytime conditions over the eastern half of the North American continent.

Approach and algorithm development. The approach used in the algorithm development includes image classification. The classification is based on specific spectral criteria. Thick ice and snow will have relatively high reflectivity in the VIS, but noticeably lower reflectivity in the MIR. It is these specific differences in spectral signatures that are the physical basis for identifying and discerning between thin and or broken ice and thicker ice. Incorporating this identification scheme may allow researchers to use historical GOES data to construct past ice classification maps.

VIS and MIR reflectance. GOES-13 channels 1 and 2, VIS (0.62 μm) and MIR (3.9 μm), are used in the development of MISI. Both snow and clouds have high reflectance values in the visible, with generally higher values for snow. Snow, thick ice, and cloud reflectances decrease with increasing wavelength in the VIS to SWIR spectrum; this decrease in reflectance is more significant with snow near 1.5 μm. The GOES imager does not operate in the 1.6 μm band; however, it does in the MIR 3.9 μm band. The daytime 3.9 μm band contains

contributions from both solar reflection and thermal emission. A significant challenge in this study is to derive the 3.9 μm solar reflective component.

Figure 2 is a comparison of GOES-13 channel spectral response for the VIS (left) and MIR (right) channels with solar spectral irradiance. The incident radiance for a particular channel is the solar spectral irradiance averaged over the spectral response for that channel:

$$R_i = \frac{\int_{\lambda_{min}}^{\lambda_{max}} S_\lambda W_\lambda \, d\lambda}{\int_{\lambda_{min}}^{\lambda_{max}} W_\lambda \, d\lambda}, \quad (1)$$

where R_i is the incident radiance (Watts/meter^2) on the channel, S_λ is the solar spectra irradiance, and W_λ is the spectral response, or weighting function of the channel's imaging sensor. The limits are determined by W_λ. For the GOES-13 VIS channel, [λ_{min}, λ_{max}] = [0.399, 1.099 μm] and for the MIR channel, [λ_{min}, λ_{max}] = [2.99, 4.99 μm].

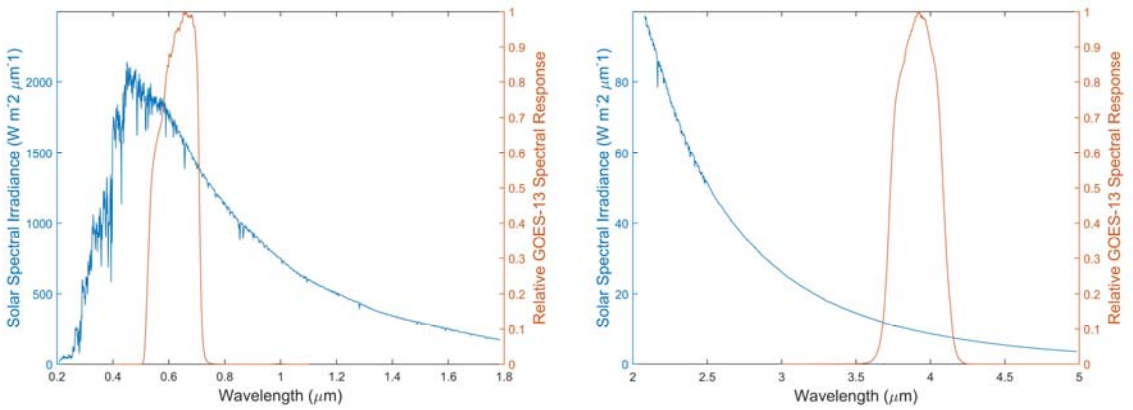

Figure 2. GOES channel spectral response and solar spectral irradiance. (**left**) 0.62 channel; (**right**) 3.9 channel.

From the data as visualized in Figure 2, R_i = 1656 W/m² for the VIS and R_i = 9.3 W/m² for the MIR. These values are an approximation using Matlab's trapezoidal numerical integration method. R_i for the VIS is in good agreement with NOAA's OSPO value of 1657 W/m² for the GOES-13 VIS channel. The calculated R_i for the MIR has not been verified, as a means of validation has not been reached; however, this value for R_i is used in this study.

R_i is the incident solar radiance within the sensor spectral band. The outgoing radiance observed by the satellite sensor is attenuated and requires a geometric correction in the VIS, which accounts for solar altitude, and atmospheric absorption correction for the MIR, which accounts for CO_2 absorption. The data has been processed with these corrections.

First the correction for the solar zenith angle is applied to VIS using a correction formula:

$$\rho = \frac{R\, d^2}{R_i \cos(\theta)}, \tag{2}$$

where R is the scene radiance as calculated from the imager data and calibration coefficients, θ is the solar zenith angle, ρ is the corrected reflectance value, and d is the Earth–Sun distance in Astronomical Units (AU). Even though this distance changes slightly throughout the year, for simplicity in this study, $d = 1$. In the remainder of this paper, ρ for VIS will be referred to as R1.

It should be apparent from Figure 2 that R_i of MIR is significantly smaller than that of the VIS. Any useful information from this R_i is more susceptible to both noise in the algorithm, a result of approximation methods, and signal noise in the sensor.

In order to derive the channel 2, 3.9 μm reflectance, the emitted component has been subtracted from the measured radiation through Planck's relation, using the channel 4, 10.7 μm, brightness temperature (BT) [14]. The full implementation of this procedure in this study is a multistep process.

The conversion of the thermal component of the MIR to radiance is:

$$R3.9_{thermal} = \frac{C_1}{\lambda^3 (e^{c_2/\lambda T} - 1)}, \tag{3}$$

The spectral radiance is a function of wavelength (λ) and the surface temperature (T). T is the $BT_{10.7}$ as derived from the inverse Planck function using the conversion coefficients of IR3.9. C_1 and C_2 are constants, 1.19×10^{-5} (mW/m^2 sr cm^{-4}) and 1.44 (K cm), respectively.

As was mentioned previously, some of the radiance in the 3.9 μm band may be lost to atmospheric absorption by the time it reaches the sensor. The primary absorber in this particular band is CO_2. Since both the reflective and thermal IR3.9 components contribute to the radiance, a CO_2 corrective coefficient is applied to both components. The CO_2 correction in the thermal may be estimated from the brightness channels of the 10.7 and 13.3 μm bands:

$$R3.9_{corr} = \frac{[BT_{10.7} - 0.25(BT_{10.7} - BT_{IR13.3})]^4}{(BT_{IR10.7})^4}, \quad (4)$$

With the correction applied:

$$R3.9_{thermal} = R3.9_{thermal}\, R3.9_{corr}, \quad (5)$$

Unlike thermal radiation, which is attenuated from surface to satellite, the radiation contributing to solar reflection is attenuated in both sun to surface and surface to satellite. This correction is estimated from the following:

$$\alpha = e^{-(1-R3.9_{corr})}\, e^{-(1-R3.9_{corr})\frac{\cos(\theta)}{\cos(\phi)}}, \quad (6)$$

The first term is the CO_2 attenuation from surface to satellite and the second term is the CO_2 attenuation from sun to surface, where θ is the solar zenith angle and ϕ is the satellite zenith angle.

Therefore, the top of atmosphere (TOA) reflectance with the CO_2 correction is:

$$TOA_{CO2\_corr} = \frac{R_i}{\pi}\cos(\theta)\ \alpha. \tag{7}$$

Finally, the reflective component of the MIR channel is:

$$\rho = \frac{R3.9 - R3.9_{thermal}}{TOA_{CO2\_corr} - R3.9_{thermal}}. \tag{8}$$

In the remainder of this paper, ρ for MIR will be referred to as R2. Equations (4)–(8) have been adopted from the European Organization for the Exploitation of Meteorological Satellites (EUMETSAT) Meteosat conversion algorithms [18].

Figure 3 presents an example of GOES Imager corrected images in VIS and MIR. Yellow areas on the Great Lakes in the 0.62 μm band image are indicative of the high reflective values of snow, thick ice, and clouds. Even though a cloud mask has not been applied, it is apparent that from the left image Lake Erie is at least partially ice covered. Some ice can also be seen on eastern Lake Superior, northern Lake Michigan, parts of Lake Huron, and eastern Lake Ontario. Blue indicates lower reflective values of water and thin/broken ice. The

right side is the derived 3.9 μm reflective. Comparison of the two images reveals a clear contrast of clouds and snow/ice. In the R2, clouds are yellow and snow/ice is deep blue. Both images shows that Lake Erie is almost completely ice covered (left) and essentially cloud free (right). Figure 4 shows 3.9 μm reflective on three different days. The middle image appears almost completely cloud-free.

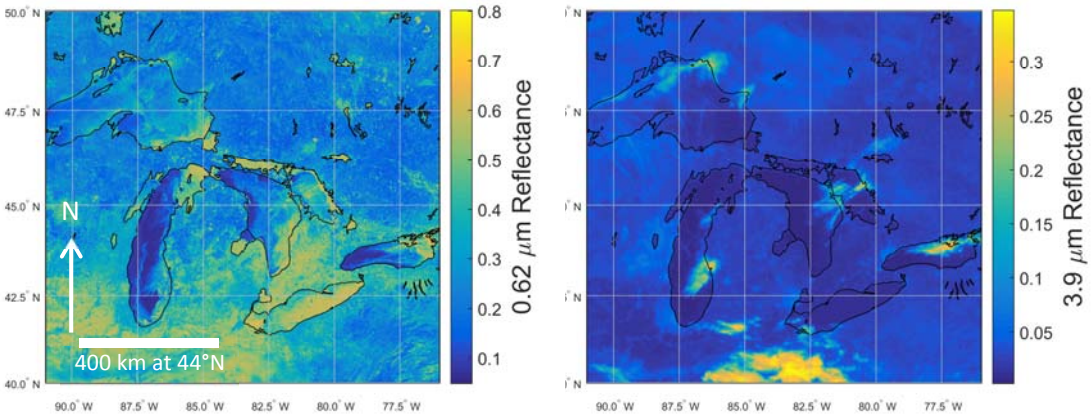

Figure 3. 0.62 μm reflectance at 1830 UTC. (**left**) 28 February 2015; (**right**) 3.9 μm reflective component.

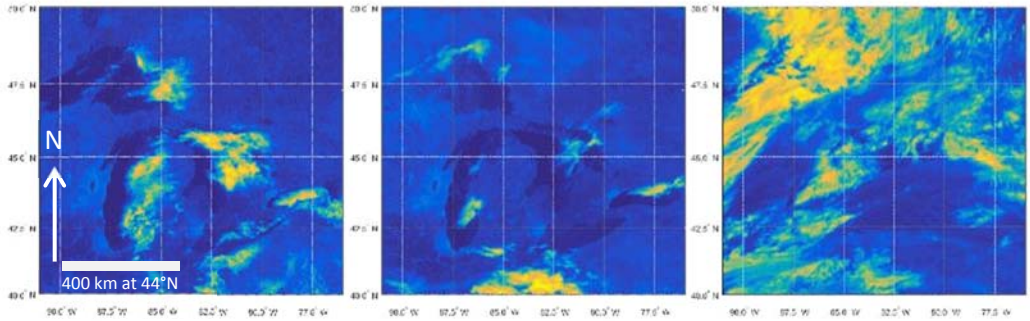

Figure 4. 3.9 μm reflective component at 1830 UTC. (**left**) 27 February 2015; (**middle**) 28 February 2015; (**right**) 1 March 2015. Bright yellows are high R2 values indicative of clouds.

Skin temperature. A single channel method is used to estimate the temperature of the emitting surface, or "skin" temperature (ST). In the absence of clouds or atmospheric attenuation, and with a surface emissivity near unity, the brightness temperature should approximately equal the skin temperature. Data from the GOES 13 channel 4 (10.7 μm) has been acquired and processed.

Within the scope of this paper, no form of atmospheric attenuation for water vapor absorption has been applied. The results of the uncorrected brightness temperature are expected to at best be marginally cooler than the actual ST.

Figure 5 illustrates the single channel method of approximating ST for Lake Michigan from GOES (left). The right figure is a surface temperature map from Michigan State University (MSU) [19]. The MSU estimates are generated from satellite sensors. The area circled on the MSU map encapsulates temperatures between 273 and 275 K. A visual comparison of these two figures shows reasonable agreement. The assumption that is made from this simple qualitative validation is that, for cold water bodies with low presence of water vapor, the single-channel method will produce a reasonable indicator of ST for classification purposes.

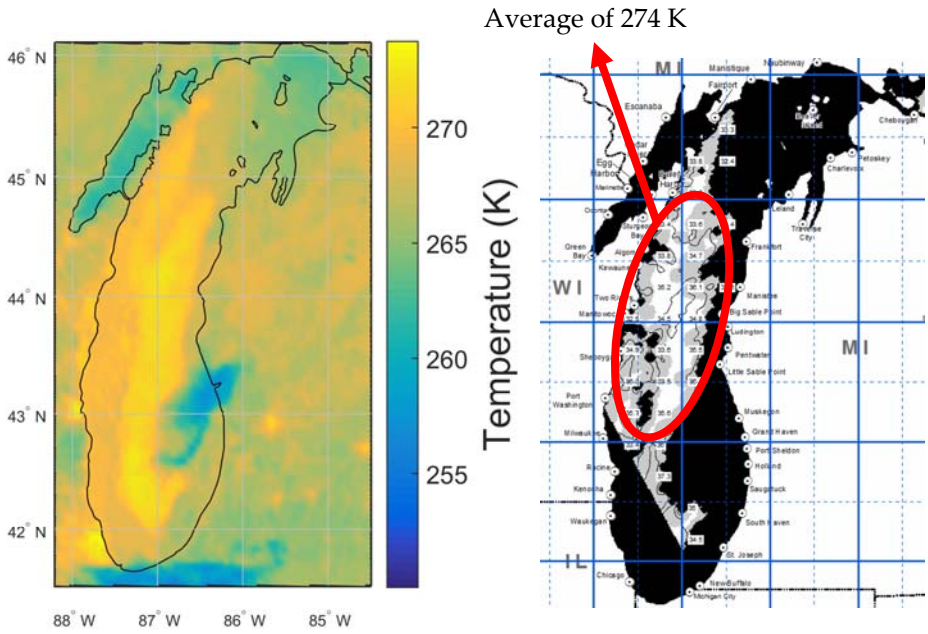

Figure 5. ST of Lake Michigan on 28 February 2015. (**left**) ST at 1730 UTC; (**right**) surface temperature map at 1754 UTC from Coastwatch at Michigan State University.

Figure 6 shows a visible image of Lake Michigan and a west-east cross-section profile of R1, R2, and ST (channel 4 brightness temperature) from the west shore until cloud coverage (approaching the east edge). A number of features are captured in this sampling: land snow, lake ice, liquid water, and cloud. The sampling is represented in the left figure by a black bar stretching from about 88° to 86.7° west longitude. The temperature for ice/liquid water is near 271 K, which is to be expected from the single-channel method. Snow land appears colder than lake ice, whereas cloud is the coldest feature in this scene.

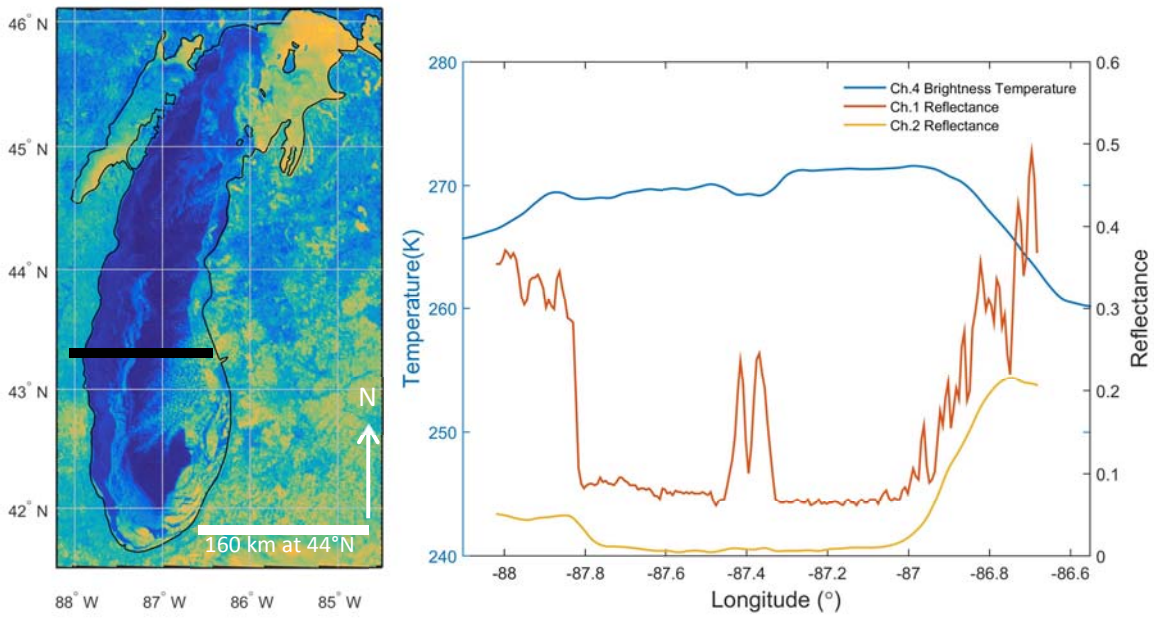

Figure 6. (**left**) 0.62 μm image of Lake Michigan at 1830 UTC on 28 February 2015. (**right**) R1, R2, ST profile along the cross section indicated by the black line on the left figure.

Water/gray ice appears along a stretch from about 88° to 87.5°, with thick ice and/or snow cover centered near about 87.4°, and again water/gray ice from 87.3° to 87°. The spectral properties of liquid water, gray ice, and "thick" ice are similar in 3.9 μm. The reflectance in the 3.9 μm is near 0.05. In the 0.62 μm channel, the reflectance of gray ice and water is just under 0.1, whereas thick ice/snow exceeds 0.1. Using a temperature threshold of 271 K to distinguish between liquid water and ice, it may also be reasonable to conclude that gray ice is more likely to be near 87.6° and liquid water near 87.2°. A more robust method to derive skin temperature should provide a value closer to 273 K. In turn, this may also help to recover some of the information lost in R2 during the

approximations. It is interesting to note that the reflectivity of R1 for gray ice approaches R2. From the above profile it is evident that R1/R2 >> 1.0 for snow or thick ice and that R1/R2 may be approaching unity for gray ice.

Snow Index. GOES NDSI using the 3.9 μm reflectance will vary within a small range close to unity. An alternative is the ratio of R1 to R2, called the snow index (SI = R1/R2) [10]. A demonstration of this is given in Figure 7. Figure 7 (left) is the snow index for Lake Michigan. The right figure is a scatter plot of the snow index and R2. The pixel sampling region (32 × 42) is indicated by the white box in the left figure. It is assumed that the sample is a mixture of water, ice, and snow. The greatest density in the scatter plot (indicated by the red oval) appears when the SI is between about 4 and 12. The sample plot appears asymptotic, with the lowest SI (R1/R2) value approaching 2.4 at a relatively high value of R2.

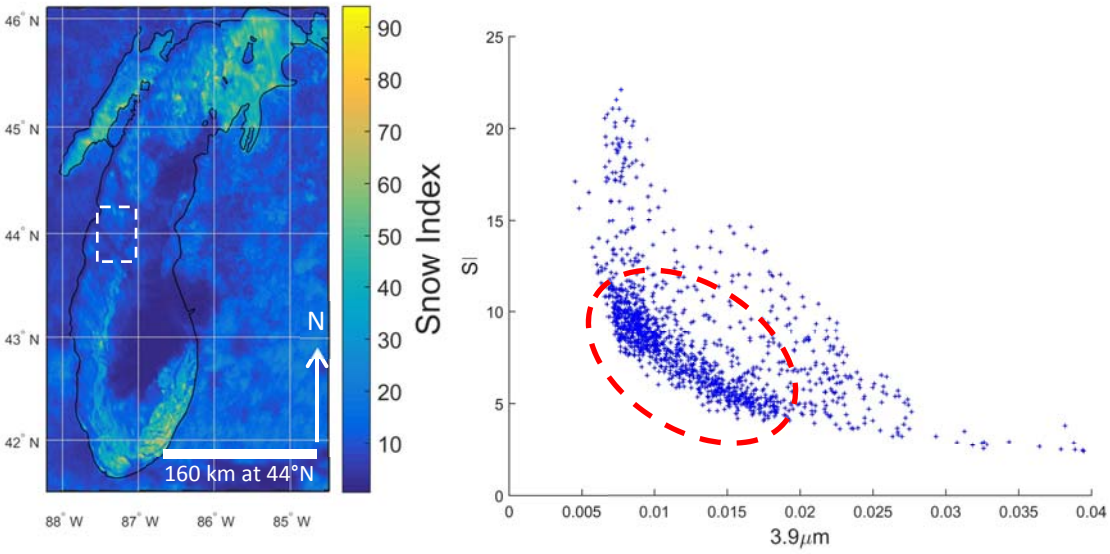

Figure 7. (**left**) Snow Index (SI) for 1830 UTC on 28 February 2015. (**right**) Scatter plot of the snow index to the 3.9 μm. The pixel sampling region (32 × 42) is indicated by the white box in the left figure.

The application of SI for lake (or sea) ice mapping is a goal of this study. Therefore, the ratio of R1/R2 as it relates to sea and lake ice mapping is referred to as MISI. The algorithm proposed in this study is a variation to the one proposed by Romanov [10]. In that study, the SI for snow is > 4.5. This seems to be in agreement with the above scatter plot, if it is assumed that the pixels encapsulated by the red circle are snow or thick ice; this dense region appears to begin near 4.5. Key relationships are the following: $R1_{\text{gray ice}} < R1_{\text{ice}}$, $R2_{\text{gray ice}} \sim R2_{\text{ice}}$ and $MISI_{\text{gray ice}} < MISI_{\text{ice}}$. "Ice" as opposed to "gray ice" refers to thick ice with or without snow cover. Unlike the MISI for snow or thick ice which will have

values significantly greater than unity, MISI values of gray ice may have values approaching unity.

Threshold Determination. The distinction between the many surface types in a scene comes from the variation in spectral properties. Here we use various thresholds in the classification scheme. The snow index and R1 thresholds were obtained from a probability distribution function for a sampling of pixels from southern Lake Michigan. The sampling consists of a mixture of water and ice pixels. 50 water pixels and 50 ice pixels were identified through a visual inspection of the visible reflectance. The data are best fit to a normal distribution, as illustrated in Figure 8 for R1 and SI (or MISI). 1830 UTC is chosen as this is close to local solar noon, minimizing the dependency of threshold values on sun-view geometry correction where the solar zenith angle is near zero. The means and standard deviations are provided in the Figures. Blue is water, and red is ice. The distributions show a clear distinction in the mean values between water and ice. The ambiguity occurs where both distributions overlap. The overlap indicates that a pixel has a probability of being water or ice. The point of intersection $P(I \cap W)$, where I is the probability of a pixel detected as ice and W is the probability of a pixel detected as water, is chosen as a threshold value for that particular time [20]. All data values above this point are classified as ice and all data values below this point are classified as water. A scatterplot for R2 did

not prove useful as both ice and water distributions almost completely overlap. This is to be expected as the R2 values for ice and water are similar (Figure 6).

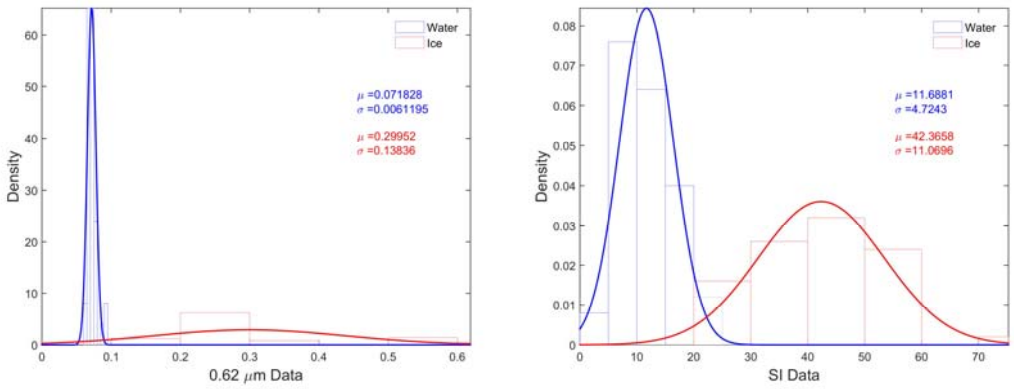

Figure 8. Probability distribution functions of water (blue) and ice (red) at 1830 UTC on 28 February 2015. (**left**) Distribution of reflectance; (**right**) distribution of snow index.

Classification Algorithm. A decision tree routine has been employed on a pixel-by-pixel basis. Figure 9 illustrates the flowchart of the developed decision tree algorithm. Ice, gray ice, water, and cloud pixels are classified. The "fixed" threshold values are applied. Thresholds for R1 (0.09), MISI (22.5) are obtain as $P(I \cap W)$ from Figure 8. The threshold for R2 (0.05) was chosen from a previous study [16]. In addition the threshold for the snow index (SI) from the previous study [16] was 4.5. From repeated observations in this study it was found that little discrimination was revealed between thick ice and gray ice with MISI

values greater than 4.5. Obtaining the threshold from the MISI PDF, seemed to provide for this discrimination.

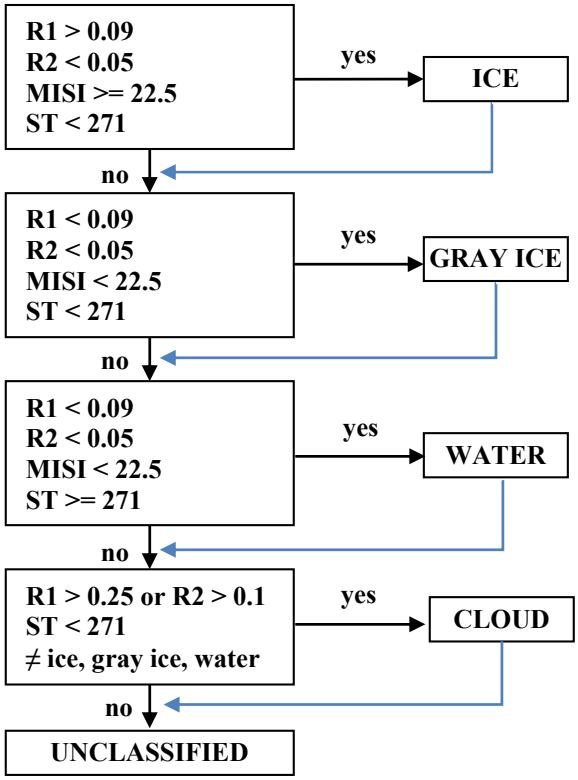

Figure 9. GOES snow/ice detection algorithm.

All pixels are first evaluated for "thick ice". The low threshold for R1 helps to insure that all forms of ice are captured (indicated by the blue arrow) prior to being evaluated for gray ice. Gray ice can be thin and or broken ice. The major criteria in discriminating between "thicker" ice from gray ice at this stage of the algorithm is based on the comparison in R1 reflectance ($R1_{ice} > R1_{gray\ ice}$) and

the R1/R2 ratio (MISI). Pixels with smaller than the threshold values of MISI are classified as gray ice. Ice pixels with the MISI value larger than the threshold are classified as thick ice. All other pixels that are not cloud, water, ice, or gray ice are unclassified. The particular threshold values for R1 and MISI in this example have been estimated from the PDFs as presented in Figure 8. It should be noted that an evaluation of data at other times, which corresponds to different solar elevations, will likely produce different thresholds. An evaluation of thresholds across all acquisition times is recommended for future work. In addition, a MISI threshold of 4.5 to delineate thick ice/gray ice was initially evaluated in the algorithm which did result in some delineation; however, there were a substantial number of unclassified pixels left in the scene. Figure 10 is a flowchart of the entire data processing method.

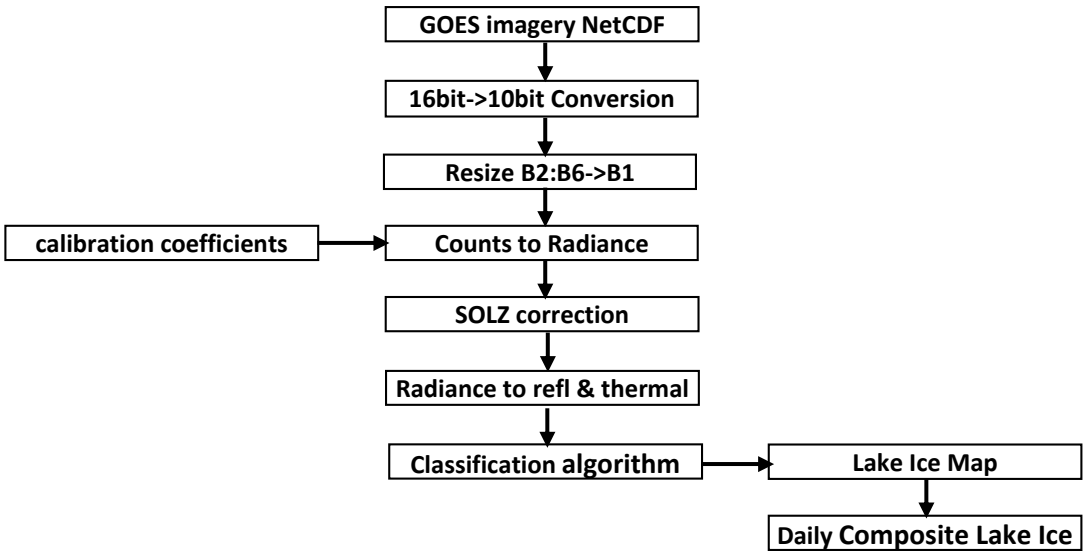

Figure 10. Data Processing.

Results

Figure 11 shows lake ice maps from 1600 UTC to 2030 UTC at half-hour increments (with the exception of 1800 UTC). The model produces four classes: water, gray ice, ice, and cloud. Unclassified pixels remain black. There are a substantial number of unclassified pixels in northwestern Lake Superior. This may be due in part to supervised threshold monitoring for this study only occurring for Lake Michigan. The thresholds were obtained from the sampling of pixels in Lake Michigan (PDF is shown in Figure 8) and simply applied to all five Great Lakes. Future work is suggested to partition the data and obtain an individual threshold for each of the Great Lakes.

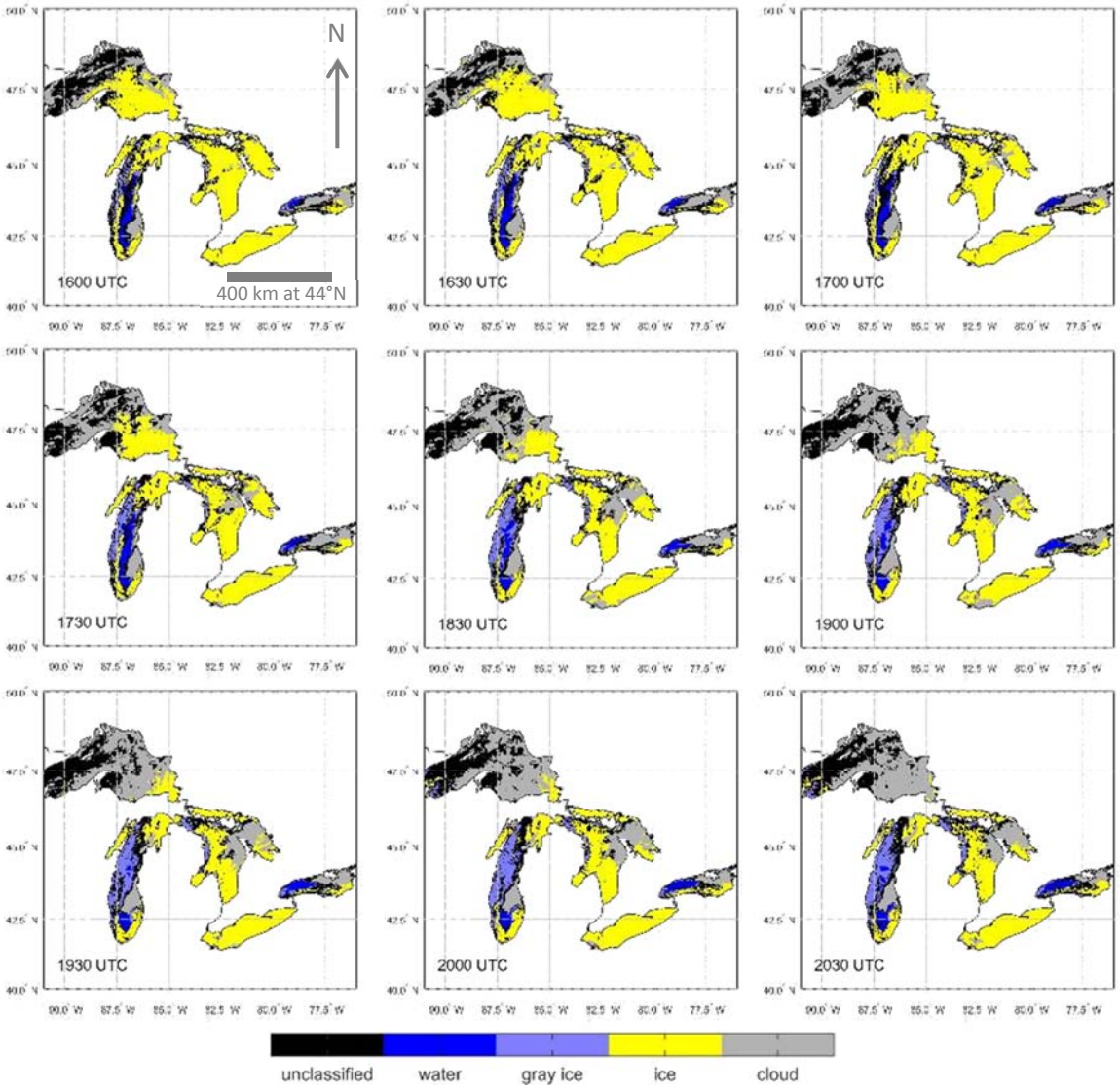

Figure 11. Lake ice maps at half-hour acquisition times (with the exception of 1800 UTC).

Figure 12 (left) is the final daily composite lake ice map. Compared with the mapping above, the daily composite map has far fewer unclassified pixels, which is clearly evident in Lake Superior. During the classification compositing process, pixels that are classified as ice or water persist. This map has been

compared with the IMS snow and ice map and shows good agreement. In addition to thick ice, the model developed in this study includes gray ice.

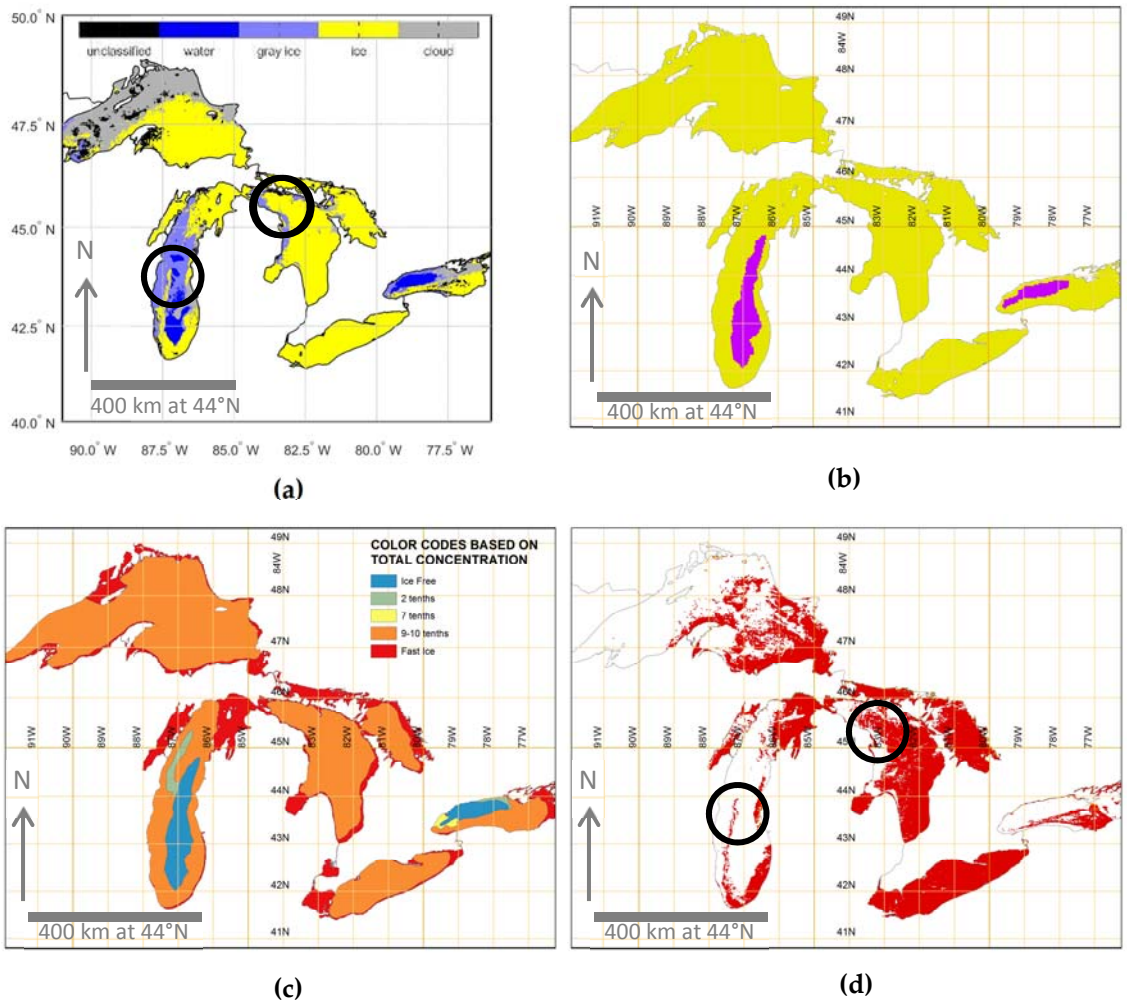

Figure 12. Various ice map products. (**a**) Lake ice daily composite map; (**b**) IMS Snow map: yellow is ice, blue is water; (**c**) National Ice Center ice concentration: blue is ice-free, red is fast ice; (**d**) MODIS snow and ice cover: red is more, yellow is less.

The bottom right image is the National Ice Center (NIC) ice concentration which encompasses a wider spectrum of ice concentrations. The interpretation of gray ice is to be inclusive of thin and/or broken ice. The bottom right image is the MODIS snow and ice product. Here, the model generally agrees with MODIS. Compared to the MODIS product, the model includes both gray and thick ice classification. Both products appear to reveal thick ice or snow extending North–South near the center of Lake Michigan, as indicated by the circles. Unlike MODIS, the model reveals gray ice along the east coast of Lake Huron, also indicated by circles. There is some discrepancy in water and ice pixels, most noticeably in Lake Michigan.

A detailed quantitative validation will be required for a more complete evaluation of the ice mapping system, including additional test scenes. Additional time-dependent threshold values for R1 and MISI are also recommended. An issue that comes up with the current version of the algorithm is that pixel classification may be overwritten during the iteration. This may be solved by implementing a binary response method in determining a particular classification for each pixel at each time. At the end of the iteration, the algorithm can simply compare the number of positive responses for each "possible" classification of each pixel and assign that pixel the classification that received the majority of positive responses.

Conclusion

Comparison of the final products with the Interactive Multisensor Snow and Ice Mapping System (IMS) maps show that the proposed model has high potential in lake ice mapping with a higher spatial resolution than IMS. While the MODIS snow product has even higher resolution, the temporal resolution of GOES-13 allows for better cloud contamination resilience. Though this study is preliminary, the model may demonstrate a more comprehensive product in that it includes both gray ice and thick ice. The mid-infrared sea and lake ice index (MISI) is the primary method for identifying gray and thick ice. MISI is the ratio of the visible reflectance to the derived reflective component of the mid-IR. From cross sectional profiles of the visible and in the mid-IR reflectance that were analyzed, thick ice and/or snow cover consistently showed higher than unity values, whereas gray ice shows values approaching unity.

One of the principle motivations of this project is to contribute to the GOES-R satellite research and product development. GOES-R, which launched in November 2016, has increased temporal and spatial resolution and includes not only the 1.6 μm band currently used in traditional NDSI snow mapping, but also a 3.9 μm band, which has been the focus of this paper for lake ice mapping. The algorithm may open up a new era in the capabilities of ice mapping systems and

climate studies using historical GOES imagery data and other satellite sensors that do not have a 1.6-μm channel.

Chapter 2

Application of Dynamic Threshold in a Lake Ice Detection Algorithm

Abstract

The traditional method involved in the classification of surface types such as water, ice, and snow rely on thresholds values that are fixed. However, the use of daily fixed thresholds leaves a substantial number of either unclassified and/or misclassified ice and water pixels. In this study, we propose a new dynamic threshold technique to identify and map lake ice cover in the imagery of GOES-I to P series satellites. In addition, dynamic threshold can be used as an alternative solution to Bidirectional Reflectance Distribution Function (BRDF) models. The technique has been applied using GOES-13 imager data over Lake Michigan, one of five of the Great Lakes. Both fixed and dynamic thresholds have been compared and a quantitative general assessment is introduced to evaluate the algorithm's performance. Implementing a dynamic threshold, can be used in constructing ice maps in applications that benefit from high temporal resolution imagery.

Introduction

With the launch of GOES-16 in November 2016, a new era of remote sensing research over the North and South Atlantic basin and adjacent land masses has begun. The primary GOES-16 instrument is the Advanced Baseline Imager capable of providing high spatial and temporal resolution data in 16 bands. The remote sensing scientific and engineering community has developed various products based on this instrument including ice and snow maps [21]. This particular study is twofold. 1) Present the use of dynamic threshold in developing a sea and lake ice map [22]; 2) Promote further the use of the GOES-13 imager in snow and ice mapping [16,23] and the potential to develop these maps using historical imagery. It is the intention of the author, that this work may contribute to the study of climate data in the Great Lakes region of which over 30 years of data from NOAA's GOES program are available.

Remote sensing based snow and ice maps for the North American region are generally limited to the short-wave infrared (SWIR) snow/ice detection bands (1.58-1.64 μm window) of certain multispectral sensors typically found on polar orbiting satellites. These include the Moderate Resolution Imaging Spectroradiometer (MODIS) on board NASA's Terra and Aqua satellites, the Advanced Very High Resolution Radiometer (AVHRR) on post NOAA-14 weather satellites, and the Visible Infrared Imaging Radiometer Suite (VIIRS)

onboard the Suomi National Polar-Orbiting Partnership (Suomi NPP) spacecraft. Use of these optical sensors for snow and ice mapping are limited to clear sky conditions. Unlike polar-orbiting satellites, the higher temporal resolution of geostationary satellites offer greater opportunity in monitoring for cloud-free conditions and pixel classification via a daily composite map. Prior to GOES-16, the GOES imagers were limited to 5 bands, none of which were in the SWIR needed for ice mapping. However, research in the use of the mid-infrared (MIR) 3.9 μm band for snow and ice maps has been investigated through the GOES imagers [16, 23].

Ice mapping products derived from polar orbiting satellites are also limited in the use of constant threshold in their algorithms [22]. For example, an ice concentration algorithm for VIIRS uses fixed threshold for the visible (vis>0.08) and (NDSI>0.45) for ice identification [11]. A reflectance threshold, as referred to in this study, is a reflectance value shared by two dissimilar surfaces (differences in spectral properties). The ambiguity that exists when classifying these surfaces is predominantly a result of the particular viewing and illumination geometry at the time of data acquisition. For example, snow has a significantly higher albedo than liquid water (difference between albedo and reflectance will be discussed in a moment). However, when sunlight reflects off the surface of a water body at the same angle that a sensor is viewing the surface

there is a significant "boost" in the reflectance of water, a phenomena known as sunglint; this can lead to classification errors while distinguishing ice from water. Ice mapping products with fixed or static thresholds that do not account for the variation in illumination geometry during the day are susceptible to these errors. Unlike polar orbiting satellites, which have low frequency of coverage offering at best a daily snapshot of the illumination geometry for a given area, geostationary satellites offer continuous coverage that allows observations across various illumination geometries. This information is useful in building a threshold that adapts to these changing lighting conditions.

The challenge for developing any surface type classification process, accounting for the ambiguity of dissimilar surfaces with overlapping spectral signatures, requires an understanding of multispectral surface reflection which depends upon both illumination and viewing direction, and is described by a particular surface's Bidirectional Reflectance Distribution Function (BRDF). Albedo is defined as the fraction of incident radiation that is reflected by a surface. The albedo of snow and ice is dependent on the solar zenith angle, θ. Reflectivity of snow and ice increases with increasing θ [24]. Albedo differs from reflectance in that albedo is the directional integration of reflectance over all possible sun-view geometries. Albedo depends on the spectral and angular distribution of incident radiation and thus is dependent on BRDF [25]. A

Lambertian surface (completely diffuse) would have a BRDF plot that is cylindrical in shape with a flat top; however, the reflectance of radiation from most natural surfaces is dependent on the sun-view geometry. Work has been done on laboratory measurements of BRDF [26], including field investigations [27] and the usefulness of these measurements in remote sensing applications. Application of laboratory measurements of BRDF on remote sensing data presents challenges including the broader scale of remote sensing instruments, complexity of physically-based BRDF models in transposing them onto remote sensing data, and the heterogeneity of land cover. These challenges have been investigated by measuring BRDF of various surface types through remote sensing instruments; including airborne [28] and geosynchronous [29] and evaluated against existing BRDF models. Today, natural surface BRDF databases exist that can be used to validate satellite sensors [28].

Dynamic threshold has been proposed in this study as an alternative to investing in a BRDF model in ice mapping algorithm. In order to build a robust and reliable ice detection algorithm, it is necessary to properly account for the effects of the variable viewing and illumination geometry of observations. Conceptually, a dynamic threshold can be an alternative solution to accounting for these effects over the use of Bidirectional Reflectance Distribution Function (BRDF) models which mathematically correct for surface reflectance anisotropy

during the classification process. As a continuation of our previous work, which provided a preliminary evaluation of the mid-infrared band to lake ice detection, here we present the results of applying a dynamic threshold. A dynamic threshold in this study is a time series of hourly reflectance thresholds based on $P(I \cap W)$, where I is the probability of a pixel detected as ice and W is the probability of a pixel detected as water. These probabilities have been derived from hourly plots of normal distributions of ice and water pixels and applied to an ice detection algorithm that uses the mid-infrared band to delineate thick ice and water. Dynamic thresholds in the visible have been used in previous studies including ice mapping which has been demonstrated over the Caspian Sea [22] and in brightness temperature for cloud detection [30].

Data and Methods

Our study area is Lake Michigan shown in Figure 13. Lake Michigan is one of five of the Great Lakes located in the northeastern Midwest United States along the U.S.–Canadian border.

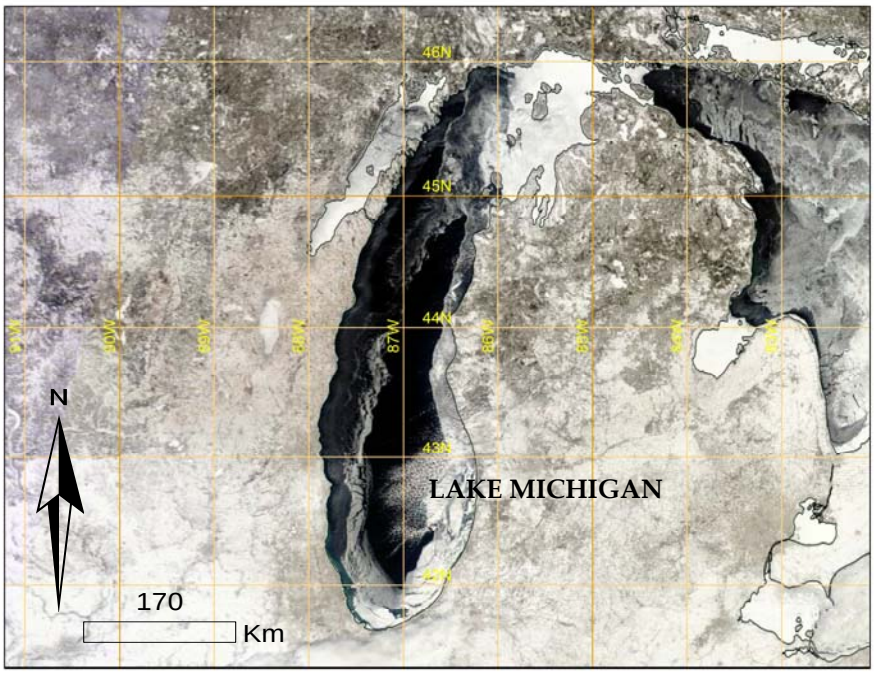

Figure 13. Ice cover on Lake Michigan. Image acquired by the Moderate Resolution Imaging Spectroradiometer (MODIS) on February 28, 2015 (NASA).

The GOES-13 satellite is in geosynchronous orbit, with a nadir located at approximately 0.05°N, 75°W. Data collected by the GOES-13 imager instrument was used in this study. The GOES imager is a five-channel instrument (one visible, four infrared), as listed in Table 1.

As this study is a continuation from previous work [23], the method for data acquisition, pre-processing, calibration and conversion, determination of skin temperature, and the derivation of the 3.9 μm reflection component has been implemented. Readers are encouraged to refer to that work for a detailed

explanation of the pre-processing and processing procedures used in the algorithm.

As in the previous study, data was acquired for February 28, 2015. Acquisition times for that day were every half-hour from 1430 UTC to 2030 UTC. These are the times that GOES-13 is in the continental US (CONUS) extended scan mode with the exclusion of near 18:00 UTC which is during the time GOES-13 is operating in full disc mode. These times also correspond to daytime conditions over the eastern half of the North American continent. The mean solar zenith angle across all scenes was 56.8° with a range from 51.73° to 70.18°.

The distinction between various surface types in a satellite image becomes possible owing to their different spectral response. Here we use an hourly threshold-based decision-tree image classification scheme to distinguish between water, gray ice, and thick ice. We refer to gray ice as thin or broken ice. The spectral properties of gray ice and thick ice are significantly different [23]. In this paper, we refer to the visible as R1 and the mid-infrared as R2. The R1, R2, mid-infrared sea and lake ice index (MISI) thresholds were determined through a visual inspection of the visible reflectance for a sampling of pixels from southern Lake Michigan. The sampling consists of a mix of water and ice pixels. 50 water pixels and 50 ice pixels were identified from each acquired image. The scene images used were rendered in gray scale. Cloud-free pixels that were relatively

dark were visually classified as water, cloud-free moderately bright to bright pixels were classified as ice. This identification of ice was visually validated against ice charts of the Great Lakes from the National Ice Center. Delineating the different ice concentrations as classified by NIC was not conducted. It should be noted that darker ice such as thin or broken ice will have reflectivity in the visible similar to water. The data is next best fitted to a normal distribution. Figure 14 are the distributions for R1, R2, and SI at 1430, 1730, 2030 UTC. Blue is water, and red is ice. The number of bins for each distribution is equal to $\sqrt{n}$. As the sampling size was relatively small, the width of the bins is relatively wide. The R1 distributions show a clear distinction in the mean value between water and ice. The ambiguity occurs where both distributions overlap. The overlapping indicates that a pixel has probability of being water or ice. For the scope of this paper, the point of intersection $P(I \cap W)$, where I is the probability of a pixel detected as ice and W is the probability of a pixel detected as water, is chosen as a threshold value for that particular time. All data values above this point are classified as ice and all data values below this point are classified as water. Since thick ice will have R1 values significantly higher than water, it is reasonable to suggest that gray ice may occur at or near $P(I \cap W)$.

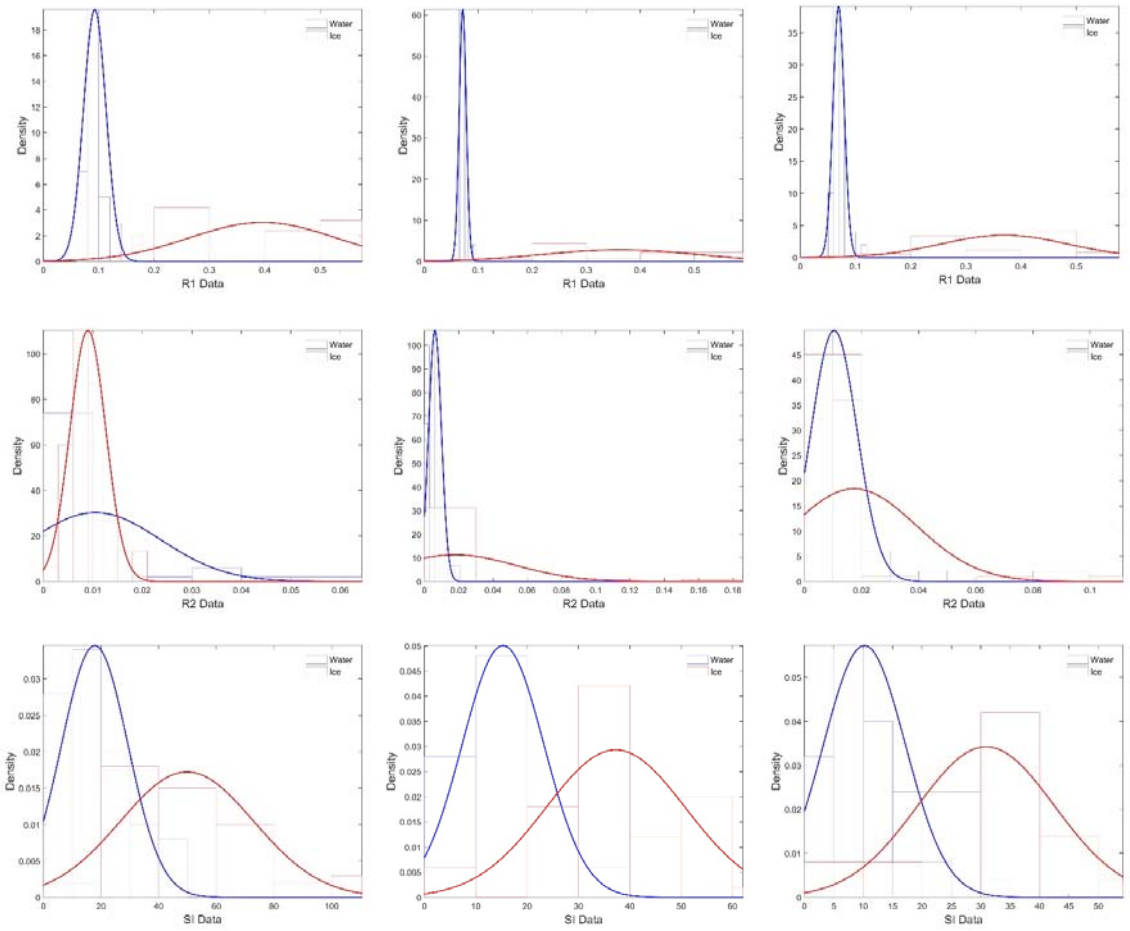

Figure 14. Probability distribution functions of water (blue) and ice (red) at 1430, 1730, 2030 UTC on February 28, 2015. (**top**) Distribution of 0.64 μm refl; (**middle**) distribution of 3.9 μm refl*10^{-1}; (**bottom**) distribution of SI.

Table 2 lists the probability threshold values for R1 (T_{r1}), R2 (T_{r2}), MISI (T_{misi}) for each acquisition time. T_{r2} is calculated: T_{r1}/T_{misi}*10. Multiplying by 10 produces T_{r2} values that are more consistent with previous studies where T_{r2} values are closer to 0.05 [16]. In addition, observation geometry is also provided: solar zenith angle (θ), solar azimuth angle (φ), solar-satellite relative azimuth

angle (γ). The observation geometry has been calculated from a point located at 43.450°N, 87.222°W. GOES-13 azimuth at this location are approximately 162.22° and 51.72° respectively. Statistical measures can be found in Appendix A, Table A.1

Table 2

Probability threshold values (T_{r1}, T_{r2}, T_{misi}) for individual acquisition times obtained from population density plots for normal distributions of ice and water.

Hour (UTC)	T_{r1}	T_{misi}	T_{r2}	θ	φ	γ
1430	0.14769	33.6477	0.044	70.18	122.94	39.28
1600	0.10119	30.8794	0.033	58.28	143.95	18.27
1630	0.088731	26.2937	0.034	55.39	152.12	10.10
1700	0.088848	28.0156	0.032	53.21	160.88	1.34
1730	0.091435	25.8933	0.035	51.83	170.08	7.86
1830	0.092061	16.5419	0.056	51.73	189.03	26.81
1900	0.08	15.523	0.051	53.01	198.27	36.05
1930	0.11904	15.1372	0.079	55.11	207.08	44.86
2000	0.12614	18.4379	0.068	57.92	215.33	53.11
2030	0.1019	33.6477	0.0302	61.36	222.97	60.75

The fixed threshold values used in the ice mapping algorithm [23] are replaced by the threshold values from Table 2. Figure 15 shows the revised detection algorithm. Sampling cloud pixels was not conducted in this study and not a goal of this study; therefore, the threshold values from the previous study for cloud identification is used.

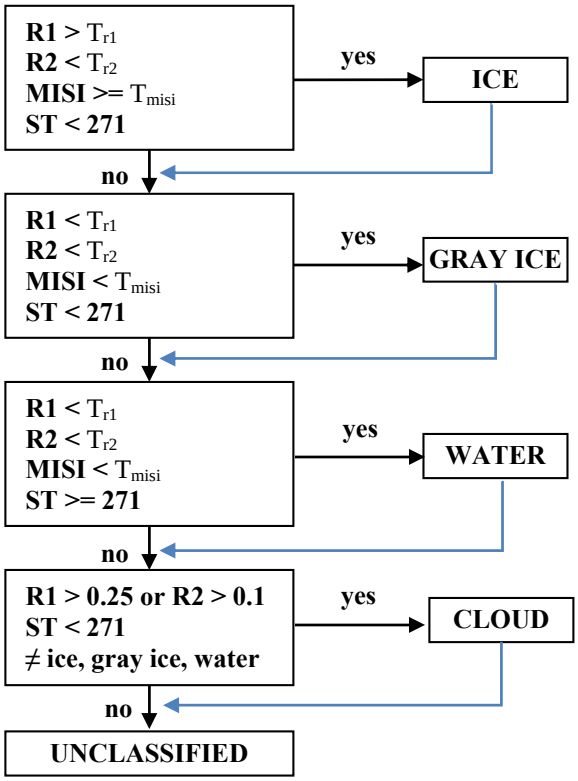

Figure 15. GOES snow/ice detection algorithm.

Figure 16 compares fixed threshold to dynamic threshold values for R1. Fixed threshold has been selected at 1730 UTC which is close to local solar noon [23]. There is high variability in the dynamic threshold values near the end of the day, this may be an artifact in the relatively small volume of the training data set.

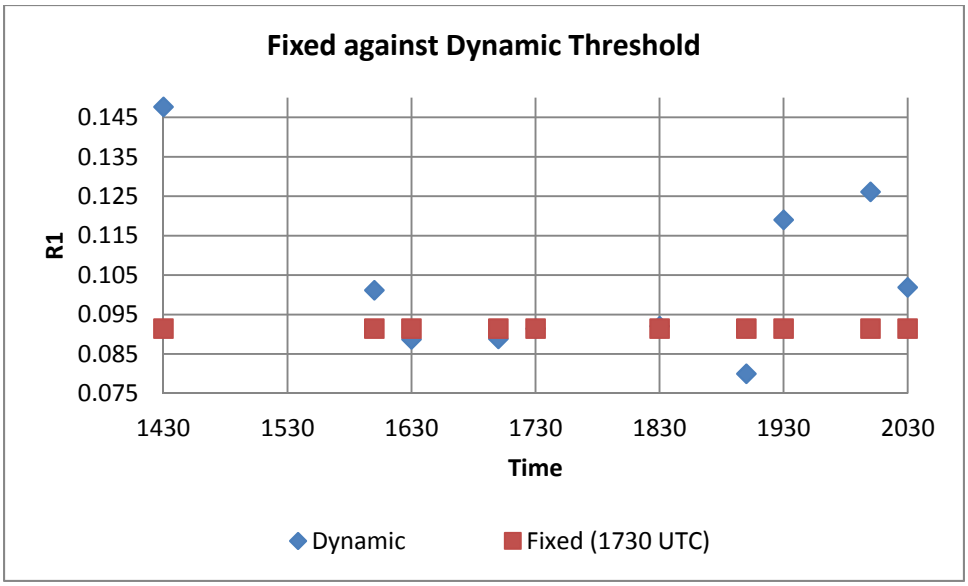

Figure 16. Fixed threshold against dynamic threshold versus acquisition times.

Results

Figure 17 compares the lake ice map generated for 1430 UTC at a fixed threshold (left) generated from 1730 UT (Figure 4) and dynamic threshold (right). A visual inspection reveals there are substantially less unclassified pixels over the lake.

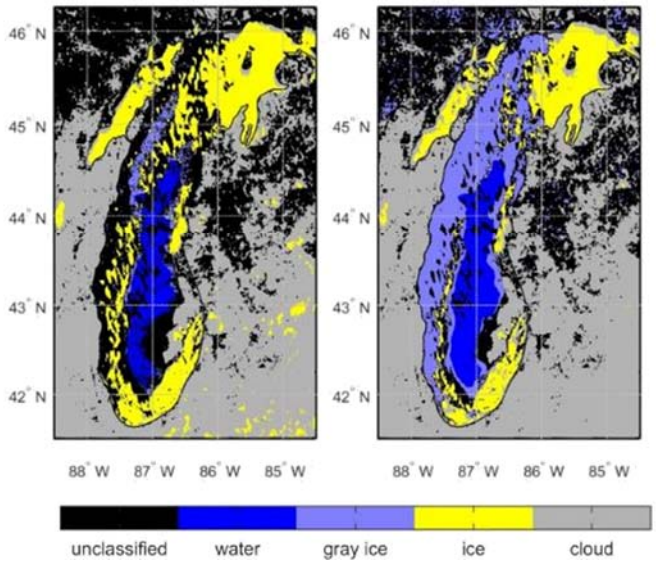

Figure 17. Lake ice map at 1430 UTC. (**left**) fixed threshold; (**right**) dynamic threshold at 1430 UTC

Figure 18 is the resulting gain of classified pixels across the ten acquisition times (Table 2) for dynamic threshold over a fixed threshold. Gain is defined as the change in the number of pixels with a positive response against the same pixels using a static threshold. The most significant gains appear to be near sunrise and sunset.

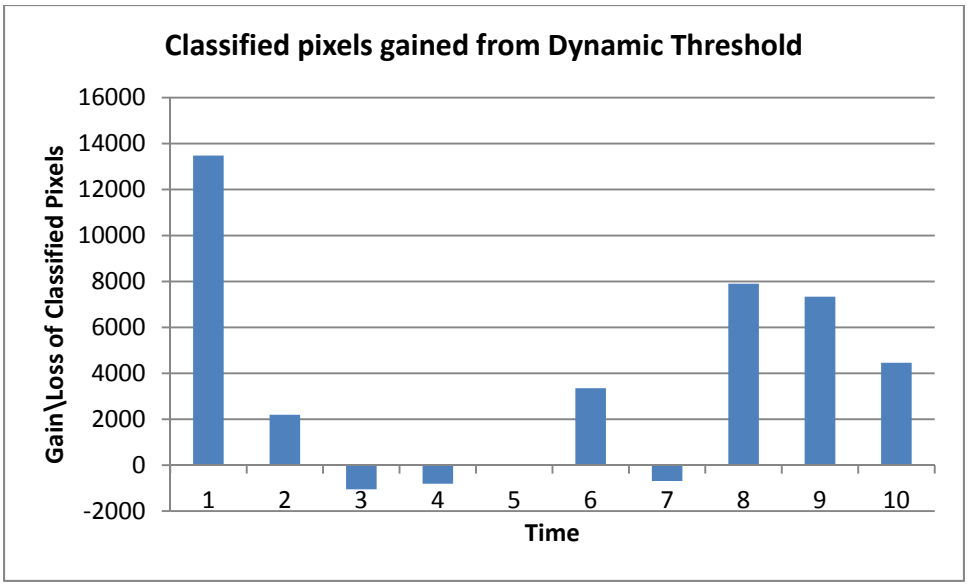

Figure 18. Dynamic threshold pixel classification gains over fixed threshold.

Figure 19 is the final daily composite lake ice map. Application of a dynamic threshold provides less unclassified pixels, resulting in a more complete ice map.

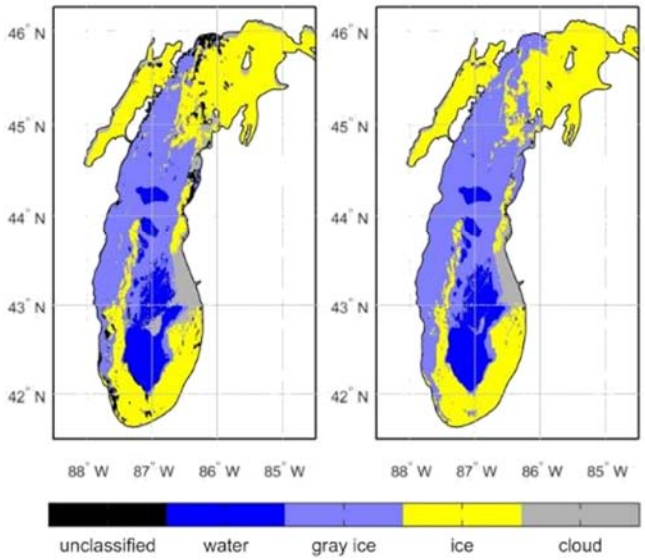

Figure 19. Lake ice daily composite. (**left**) fixed threshold; (**right**) dynamic threshold

Performance Evaluation

At this point, the application of dynamic threshold for this particular scene has resulted in substantially fewer unclassified pixels. The next step is to test the performance of the algorithm in its ability to delineate ice and water. The use of spatial analysis methods commonly used in Geographic Information System (GIS) has been used to quantify this performance.

ESRI ArcGIS (10.2.1) is used in validating the classified pixels against Interactive Multisensor Snow and Ice Mapping System (IMS) and NIC ice maps. Vector and raster data are the two basic spatial data types used in GIS. Vector data are comprised of vertices and paths. Vertices can be used to construct lines

and polygons (areas). The simplest vector data – vector points – are XY coordinates. Vector data are stored as XY coordinate pairs (latitude and longitude). Raster data are comprised of pixels (grid cells). Each pixel is associated with a value. Discrete rasters have distinct categories. These data may be stored as integer values to represent classes. For example, in land or surface cover, a value of 4 may represent snow, a value of 3 may represent sea ice. Raster data may be stored in the GeoTIFF file format which allows georeferencing information to be embedded within a TIFF file. Raster data can be converted into vector data which may then be stored as a shapefile. The shapefile format is developed and regulated by ESRI and allows geospatial data to be shared across multiple GIS platforms.

The U.S. National Ice Center provide ice and snow products in various formats including geotiff and shapefiles. In this study, the IMS data is obtained as a geotiff and the NIC ice concentration map is obtained as a shapefile. The MISI classification data stored as a matrix in Matlab is converted to vector data for use in GIS.

There are multiple techniques in performing quantitative analysis in GIS. The process of validation in this study involves testing a MISI pixel class that satisfies a boundary condition derived from the IMS and NIC maps that best

represents the class. This decision boundary will be referred to as a catchment area. For the IMS, this is done by vectorizing the input raster. The process of vectoring a raster is shown in Figure 20. The polygons conform exactly to the raster's cell edges (non-simplified output). This method should work well as IMS classifications are relatively homogeneous.

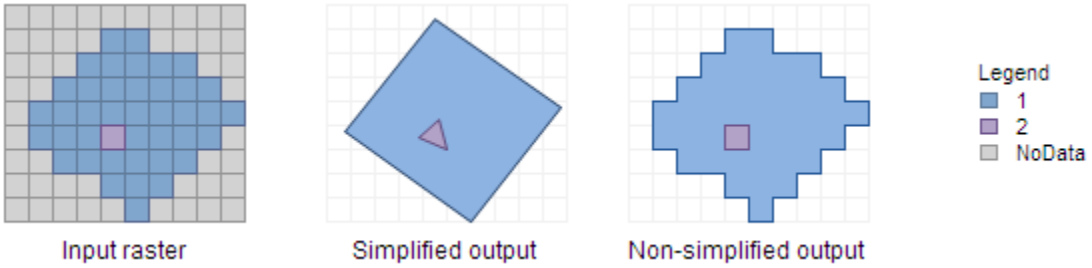

Figure 20. Process of vectorizing raster data. (Used with permission. Copyright © 2017 Esri. All rights reserved.)

Table 3 presents the classification scheme of this model (MISI), IMS, and NIC. The MISI values are the classes and the IMS and NIC are values of the catchment areas. CT is total concentration.

Table 3

Classification values for three products.

MISI	IMS	NIC (CT Codes)
2 Water	1 Water	00 Ice Free
3 Gray Ice	3 Ice	20 Young Ice
4 Snow/Thick Ice	4 Snow	91 Medium 1st Year Ice
5 Cloud		92 Fast Ice

To prepare for analysis in GIS, the classification map was down-sampled to a resolution of $(4km)^2$/pixel. The resulting 3440 test pixels ($16km^2$/pixel) total area of coverage is 55,040 km^2 (Lake Michigan is approximately 58000 km^2). The 3440 test pixels that fall within the Lake Michigan boundary are spatially queried and checked for containment within each catchment area. Figure 21 shows the IMS ice catchment area in red and water catchment area in light blue (**a**). All MISI pixels are queried within the ice catchment (**b**); and within the water catchment (**c**).

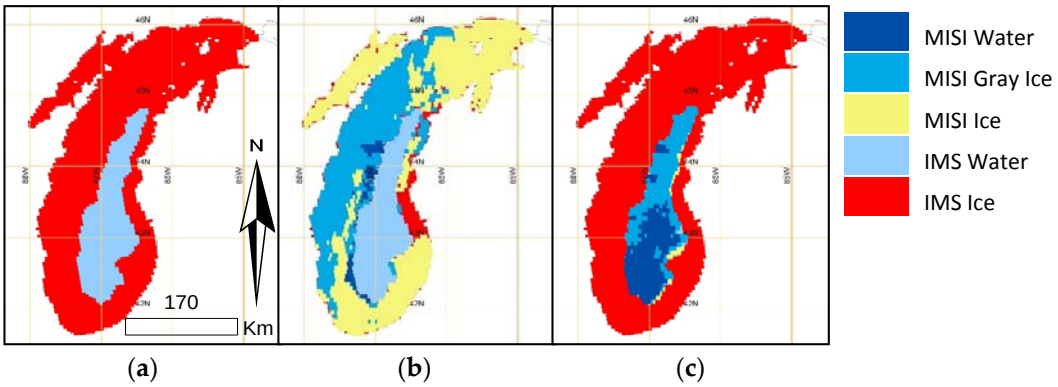

Figure 21. **(a)** IMS ice catchment area in red and water catchment area in blue. Spatial query of MISI pixels within **(b)** IMS ice area; **(c)** IMS water area

The percentage of MISI pixels classified within each IMS catchment area are tabulated (Table 4). 2.56% remain unclassified. For the IMS product, the ice/water numerical fraction is 78.97%/20.35%; MISI product is 70.3%/12.61%.

Table 4

Percentage of MISI classified pixels within IMS catchment areas.

	Snow/Thick Ice	Gray Ice	Water	Cloud
IMS Ice	40.98%	29.33%	2.5%	3.95%
IMS Water	0.75%	9.27%	10.11%	0.55%

Here we discuss the performance of the classification. Sensitivity and specificity are statistical measures of the performance of a binary classifier. The binary test in this case, is a whether a pixel is ice or not. If the pixel is not ice than it is classified as water. For this evaluation, sensitivity measures the proportion of actual lake ice pixels which are correctly identified. Specificity measures the proportion water pixels that are correctly identified. Table 5 presents a breakdown of these measurements.

Table 5

MISI Performance evaluation in IMS ice prediction using sensitivity and specificity tests.

		MISI Ice Prediction		
IMS Ice		snow/thick ice	snow/thick/gray ice	water
T E	ice	(TP) = 1410 (40.98%)	(TP) = 2419 (40.98%+29.33%)	(FP) = 86 (2.5%)
S T	water	(FN) = 26 (0.75%)	(FN) = 345 (0.75%+9.27%)	(TN) = 348 (10.11%)
		sens = 1410/(1410+26) = 0.98	sens = 2419/(2419+345) = 0.87	spec = 348/(348+86) = 0.80
		Accuracy = 94.01%	Accuracy = 86.52%	

From the performance evaluation table, the inclusion of gray ice in the classification results in lower performance (86.52%) than without it (94.01%). This

is due to the ambiguity that exists between cold water and gray ice. Both gray ice and water have similar reflectivity and the only ice-water discrimination that occurs in the algorithm is from the skin temperature [23]; therefore, there are a significant number of misclassified water pixels as gray ice (Figure 9c).

NIC provides a more comprehensive ice concentrations delineation. The MISI model is compared. Figure 22 shows the NIC catchment areas for various ice concentrations (a). All MISI pixels are queried within fast sea ice catchment (b); within the medium 1st year ice catchment (c); and within the ice free catchment.

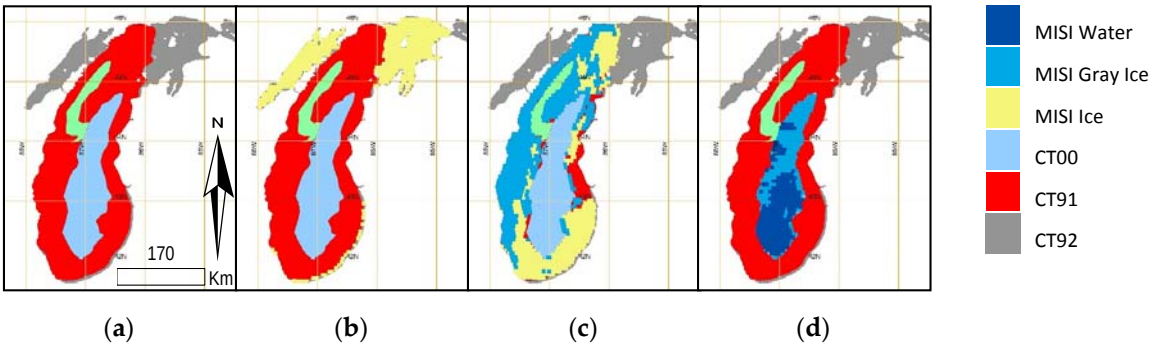

Figure 22. **(a)** NIC catchment areas. Spatial query of MISI pixels within **(b)** NIC CT92; **(c)** NIC CT91; (**d**) NIC CT00

The percentage of MISI pixels classified within each NIC catchment area are tabulated (Table 6). The table shows a possible delineation of thick ice and grey ice outside the medium 1st year ice catchment area. A binary test against the NIC map is proposed for future work.

Table 6

Percentage of MISI classified pixels within NIC catchment areas.

	Snow/Thick Ice	**Gray Ice**	**Water**	**Cloud**
NIC 00 Ice Free	0.2%	9.68%	11.19%	0.17%
NIC 20 Young Ice	0.03%	3.89%	0.049%	0.03%
NIC 91 Medium 1st Year Ice	23.17%	24.48%	1.02%	3.89%
NIC 92 Fast Ice	18.49%	0.23%	0.03%	0.38%

Conclusion

A dynamic threshold is an alternative to Bidirectional Reflectance Distribution Function (BRDF) correction which accounts for the biophysical, reflectance, and specular properties of a surface. In this study, a dynamic threshold based on lake ice detection method using an hourly threshold is developed. The threshold values are calculated on an hourly basis and applied to an ice detection algorithm through each iteration. The algorithm has been applied over Lake Michigan, one of five of the Great Lakes. Both fixed and

dynamic thresholds have been compared. The resulting composite map using dynamic threshold yields significantly less unclassified pixels then the composite map using fixed threshold. A general quantitative evaluation of the algorithm against IMS reveals good performance when delineating thick ice from water but lower performance when delineating gray ice from water. The use of a dynamic threshold can be used in constructing ice maps in applications that require higher temporal resolution. Future work proposed in this area includes additional yearly test scenes of the same region in identical solar-view geometries to validate the robustness of the dynamic threshold followed by the development of additional dynamic threshold for other solar-view geometries, again in the same region.

References

[1] *Ice formation* [Online]. Available: https://nsidc.org/cryosphere/seaice/characteristics/formation.html.

[2] Q. Zeng, M. Cao, X. Feng, F. Liang, X. Chen, W. Sheng, "A study of spectral reflection characteristics for snow, ice and water in the north of China", *Hydrol. Appl. Remote Sens. Remote Data Transm,* vol. 145, pp. 451–462, 1984

[3] J. Salisbury, D. D'Aria and A. Wald, "Measurements of thermal infrared spectral reflectance of frost, snow, and ice", *Journal of Geophysical Research: Solid Earth*, vol. 99, no. 12, pp. 24235-24240, 1994.

[4] D. Perovich, "The Optical Properties of Sea Ice", *MONO-96–1*, Army Cold Regions Research and Engineering Lab: Hanover NH, USA, 1996; pp. 8–9.

[5] D. Perovich, "The Optical Properties of Young Sea Ice", *SCIENTIFIC-17*, Washington Univ Seattle Dept of Atmospheric Sciences: Seattle, WA, USA, 1979; p. 71.

[6] D. Perovich, C. Roesler and W. Pegau, "Variability in Arctic sea ice optical properties", *Journal of Geophysical Research: Oceans*, vol. 103, no. 1, pp. 1193-1208, 1998.

[7] F. Valovcin, "Snow/Cloud Discrimination", *AFGL-TR-76–0174*, Air Force Geophysics Lab, Hanscom AFB: Bedford, MA, USA, 1976, p.13.

[8] H. Kyle, R. Curran, W. Barnes, D. Escoe, "A cloud physics radiometer", in *Proceedings of the 3rd Conference on Atmospheric Radiation*, MA, 1978, pp. 107–109.

[9] J. Dozier, "Spectral signature of alpine snow cover from the landsat thematic mapper", *Remote Sensing of Environment*, vol. 28, pp. 9-22, 1989.

[10] D. Hall, G. Riggs and V. Salomonson, "Development of methods for mapping global snow cover using moderate resolution imaging spectroradiometer data", *Remote Sensing of Environment*, vol. 54, no. 2, pp. 127-140, 1995.

[11] Y. Liu, J. Key and R. Mahoney, "Sea and Freshwater Ice Concentration from VIIRS on Suomi NPP and the Future JPSS Satellites", *Remote Sensing*, vol. 8, no. 6, p. 523, 2016.

[12] G. Riggs, D. Hall, "Snow mapping with the MODIS Aqua instrument", in *Proceedings of the 61st Eastern Snow Conference*, ME, 2004, pp. 9-11

[13] M. Haq, K. Jain, K. Menon, "Development of new thermal ratio index for snow/ice identification", *Int. J. Soft Comput. Eng.*, vol. 1, pp. 2231–2307, 2012

[14] R. Allen, P. Durkee and C. Wash, "Snow/Cloud Discrimination with Multispectral Satellite Measurements", *Journal of Applied Meteorology*, vol. 29, no. 10, pp. 994-1004, 1990.

[15] J. Key and R. Barry, "Cloud cover analysis with Arctic AVHRR data: 1. Cloud detection", *Journal of Geophysical Research*, vol. 94, no. 15, p. 18521, 1989.

[16] P. Romanov, G. Gutman and I. Csiszar, "Automated Monitoring of Snow Cover over North America with Multispectral Satellite Data", *Journal of Applied Meteorology*, vol. 39, no. 11, pp. 1866-1880, 2000.

[17] J. Lee, C. Chung, M. Ou, "Evaluation of the Geostationary Satellite Based Snow and Sea Ice Detection Algorithm", *Gisangcheong-gil 45*, Seoul, Korea, 2015.

[18] *Introduction to MSG Channels* [Online]. Available: http://oiswww.eumetsat.org/WEBOPS/msg_interpretation/msg_channels.php.

[19] *Michigan Sea Grant Coastwatch. Lake Michigan Surface Temperature* [Online]. Available: http://www.coastwatch.msu.edu/michigan/archive/m/Feb28/2015_Feb28_1254EDT.gif.

[20] H. Ghedira, R. Khanbilvardi, P. Romanov, "Development of an advanced technique for mapping and monitoring sea and lake ice for the future GOES-R Advanced Baseline Imager (ABI)", in *Proceedings of the 2007 IEEE International Geoscience and Remote Sensing Symposium*, Barcelona, Spain, 2007, pp.4241-4244

[21] R. Nazari, R. Khanbilvardi, & Cryosphere, N. C., "Fractional Ice mapping and monitoring for the future GOES-R Advanced Baseline Imager (ABI)", *AGU Fall Meeting Abstracts*, 2011.

[22] R. Nazari and R. Khanbilvardi, "Application of dynamic threshold in sea and lake ice mapping and monitoring", *International Journal of Hydrology Science and Technology*, vol. 1, no. 12, p. 37, 2011.

[23] P. Dorofy, R. Nazari, P. Romanov and J. Key, "Development of a Mid-Infrared Sea and Lake Ice Index (MISI) Using the GOES Imager", *Remote Sensing*, vol. 8, no. 12, p. 1015, 2016.

[24] P. Singh, *Snow and glacier hydrology*. Dordrecht: Springer, 2011.

[25] *Retrieval of surface albedo from space* [Online]. Available: http://www2.hawaii.edu/~jmaurer/albedo/.

[26] S. Sandmeier and A. Strahler, "BRDF laboratory measurements", *Remote Sensing Reviews*, vol. 18, no. 2-4, pp. 481-502, 2000.

[27] M. Dumont, O. Brissaud, G. Picard, B. Schmitt, J. Gallet and Y. Arnaud, "High-accuracy measurements of snow Bidirectional Reflectance Distribution Function at visible and NIR wavelengths – comparison with modelling results", *Atmospheric Chemistry and Physics*, vol. 10, no. 5, pp. 2507-2520, 2010.

[28] C. Gatebe and M. King, "Airborne spectral BRDF of various surface types (ocean, vegetation, snow, desert, wetlands, cloud decks, smoke layers) for remote sensing applications", *Remote Sensing of Environment*, vol. 179, pp. 131-148, 2016.

[29] K. Noguchi, A. Richter, V. Rozanov, A. Rozanov, J. Burrows, H. Irie, K. Kita, "Effect of surface BRDF of various land cover types on geostationary observations of tropospheric NO_2", *Atmospheric Measurement Techniques*, vol. 7, pp. 3497-3508, 2014.

[30] X. Daxiang, T. Debao, W. Xiongfei and W. Qiao, "A Dynamic Threshold Cloud Detecting Approach based on the Brightness Temperature from FY-2 VISSR Data", *ISPRS - International Archives of the Photogrammetry, Remote Sensing and Spatial Information Sciences*, vol. 73, pp. 617-625, 2015.

Appendix A

Statistical Measures

Table A.1

Estimated means, standard deviations, and probability threshold values for individual acquisition times obtained from population density plots for normal distributions of ice and water.

R1					
Hour (UTC)	μ_{water}	σ_{water}	μ_{ice}	σ_{ice}	Threshold
1430	0.092741	0.020367	0.39584	0.1317	0.14769
1600	0.078045	0.008	0.315533	0.12695	0.10119
1630	0.071552	0.005382	0.34496	0.13192	0.088731
1700	0.072972	0.004917	0.3538	0.13588	0.088848
1730	0.071051	0.006507	0.3623	0.14181	0.091435
1830	0.069401	0.00745	0.33907	0.1319	0.092061
1900	0.065975	0.00399	0.31204	0.13405	0.08
1930	0.076473	0.013914	0.3681	0.10879	0.11904
2000	0.075928	0.017539	0.36078	0.11037	0.12614
2030	0.069172	0.01021	0.36934	0.11445	0.1019
MISI					
Hour (UTC)	μ_{water}	σ_{water}	μ_{ice}	σ_{ice}	Threshold
1430	17.8176	11.5313	49.8406	23.1565	33.6477
1600	18.3313	11.7336	42.5742	15.797	30.8794
1630	14.9961	6.3675	41.6562	10.4675	26.2937
1700	16.8697	8.305	39.8668	14.9251	28.0156
1730	15.3051	7.9683	37.2434	13.6165	25.8933
1830	8.0109	3.5293	39.5333	12.6842	16.5419
1900	7.5638	3.678	35.8621	14.7138	15.523
1930	5.9785	5.0384	30.7143	18.2177	15.1372
2000	7.972	6.7128	30.5533	18.0781	18.4379
2030	10.2028	6.9713	30.882	11.6634	19.8654

Table A.2

Number of classified pixels gained with fixed against hourly thresholds.

Hour (UTC)	fixed(1730)	hourly	diff
1430	54368	40885	13483
1600	40441	38244	2197
1630	34001	35055	-1054
1700	30568	31373	-805

Hour (UTC)	fixed(1730)	hourly	diff
1730	32366	32366	0
1830	39921	36567	3354
1900	42024	42712	-688
1930	44605	36703	7902
2000	47666	40329	7337
2030	52187	47729	4458
Composite	12888	9184	3704

Appendix B

Matlab Code

```
%%%%%Main1%%%%
buildclassmap=1;
 %timeSnow(9)=0;
files_02_28_15;

%fn = 'goes13.2015.059.173018.BAND_';
%fn = 'goes13.2015.058.173019.BAND_';
%fn = 'goes13.2015.058.203019.BAND_';
maptitle = strcat('Composite',' UTC');

fixed = 0;
for c = 1:1
   fn = files{c};


   if fixed == 1
   thr = 'fixed';
   %R1Thres = 0.09;
   %SIThres = 22.5;
   %R2Thres = 0.05;

   %Threshold for 1730
   R1Thres = 0.091435;
   SIThres = 25.8933;
   R2Thres = R1Thres/SIThres*10;
   end

   if fixed == 0
   thr = 'dynamic';
   R1Thres = R1threshold(c);
   SIThres = SIthreshold(c);
   R2Thres = (R1Thres/SIThres)*10;
   end



   FetchDataNetCDF;
   Resize;
   SatSolZenith;
   Convert16to10bit;
```

```
   GVARCountToRadiance;
   RadianceToTemperature;
   SWIRtoRefl;

   Algorithm1;

   maxLat = max(latitude(:));
   minLat = min(latitude(:));
   maxLon = max(longitude(:));
   minLon = min(longitude(:));


   %MapItNew('R2','Reflectance',1,R2,latitude,longitude,0);
   %MapItNew('T4','Temperature',1,T4,latitude,longitude,0);
   %MapItNew('SI','Snow Index',1,SI,latitude,longitude,0);
   %ExcelImport; %Find Threshold

  % CrossSection;
  % mode=1;ChannelCorrelations;

end

%SI(SI>100.0)=100;

%title='Ch2_Refl_1830_lakeMichigan';MapItNew('R2','3.9\mumReflectance',1,R2,latitude,lon
gitude,0,1,title);
%title='Ch2_Refl_1830_03_01';MapItNew('R2','3.9\mumReflectance',1,R2,latitude,longitude,
0,0,title);
%title = 'Ch4_BT_1730';MapItNew('T4','Temperature (K)',1,T4,latitude,longitude,0,6,title);
%title = 'SI_1830';MapItNew('SI','Snow Index',1,SI,latitude,longitude,1,0,title)
%title = 'SI_1830_colobar_lakeMichigan';MapItNew('SI','Snow
Index',1,SI,latitude,longitude,0,6,title)


%SSTf = T4.*(9/5)-459.67;
%figure('name',figtitle);
%imagesc(R1);
%set(gcf,'position',[0 0 1000 1000]) % sets figure size


%temp1 = pi*r1;
%temp2 = 1657*cSOLZ;
%R1 = temp1 ./ temp2;
%R1 = (pi*r1)./(1657*cSOLZ);

%rMax = max(R1(:));
%rMin = min(R1(:));
```

```
%r2Max = max(R2(:));
%r2Min = min(R2(:));

%plot(R1,R2);

%r1 = R1(:);
%r2 = R2(:);
%n = [r1,r2];
%R = georasterref('RasterSize',[876 2732],...
%    'RasterInterpretation','cells','ColumnsStartFrom','north',...
%    'RowsStartFrom','west','LatitudeLimits',[37.7043 51.7789],'LongitudeLimits',[-99.0046 –
73.7185]);

if buildclassmap==1
baseicemap = shaperead('arcgis\data\northamericamask\northamericamask1.shp',
'UseGeoCoords', true);
basemap = shaperead('arcgis\data\ne_10m_lakes\ne_10m_lakes.shp', 'UseGeoCoords',
true);
maptitle = strcat(num2str(hour),num2str(minute),' UTC','_',thr);
%maptitle = '2030 UTC';
SeaIceMap(latitude,longitude,Class,baseicemap,maptitle,1);
%ClassificationMap(latitude,longitude,Class,basemap,maptitle);
end

%[a,b]=hist(Class,unique(Class));
%t = tabulate(Class);
%counts1 = t(t(:,2)~=0, 2);

%Counts = accumarray(Class,1)  %# Will return a 7-by-1 vector
%lat1(5,5)=40;
%lon1(5,5)=90;
%cls(5,5)=0;
%cls(5,4)=6;
%cls(3,4)=6;
%cls(5,5)=6;
%isUnclassified(5,5)=0;
%isUnclassified(lat1>39 & lon1>80 & cls==6)=1;
%list = isUnclassified(:);
%cts_unclassified = sum(list==1);


%list = Class(:);
%lat1 = latitude(:);
%lon1 = longitude(:);

%ax = worldmap([41.50 46.25], [-88.50 -84.50]); %lake michigan

%Class(lat1>=41.50
```

```
%cts_unclassified = sum(list==0);

%lat1(5,5)=40;
%lon1(5,5)=90;
%cls(5,5)=0;
%cls(5,4)=6;
%cls(3,4)=6;
%cls(5,5)=6;
%isUnclassified(5,5)=0;
%isUnclassified(lat1>39 & lon1>80 & cls==6)=1;
%list = isUnclassified(:);
%cts_unclassified = sum(list==1);
countunclassified =0;
if countunclassified ==1
isUnclassified=zeros(sizeX,sizeY);
isUnclassified(latitude>=41.50 & latitude<=46.25 & longitude>=-88.50 & longitude<=-84.50 &
Class==0)=1;
list = isUnclassified(:);
cts = sum(list==1)
end
Class=Class(:);
latitude = latitude(:);
longtitude = longitude(:);



%--------------------FetchDataNetCDF--------------------

%Get Size
fn = strcat('study areas\great lakes\goes13\data\',fn);
src = strcat(fn,'02.nc');
ncid = netcdf.open(src,'NC_NOWRITE');
[numdims,nvars,natts] = netcdf.inq(ncid);
[dimxname, dimxlength] = netcdf.inqDim(ncid, 0);
[dimyname, dimylength] = netcdf.inqDim(ncid, 1);

%info = ncinfo(src);
date = ncread(src, '/crDate')';
time = ncread(src, '/crTime')';
latitude = ncread(src, '/lat')';
longitude = ncread(src, '/lon')';

band = '01.nc'; src = strcat(fn,band); x1 = ncread(src, '/data')';
band = '02.nc'; src = strcat(fn,band); x2 = ncread(src, '/data')';
band = '03.nc'; src = strcat(fn,band); x3 = ncread(src, '/data')';
band = '04.nc'; src = strcat(fn,band); x4 = ncread(src, '/data')';
band = '06.nc'; src = strcat(fn,band); x6 = ncread(src, '/data')';
```

```
%--------------------Resize--------------------

targetSize = [dimylength dimxlength];
x1 = imresize(x1, targetSize);

%x2 = imresize(x2, targetSize);
%x3 = imresize(x3, targetSize);
%x4 = imresize(x4, targetSize);
%x6 = imresize(x6, targetSize);


%--------------------SatSolZenith--------------------

sTime = int2str(time);
hour = str2num(sTime(1:2));
minute = str2num(sTime(3:4));

t(1)=year;t(2)=month;t(3)=day;t(4)=hour+ut_offset;t(5)=minute;t(6)=0;t(7)=ut_offset; %ex:1730-
5=1230

location.longitude = longitude;
location.latitude = latitude;
location.altitude = 1;
SOL = sun_position_My(t,location,t(7));
SENZ = SatZ(latitude,longitude);
cSOLZ = cos(SOL.zenith*pi/180);

%--------------------Convert16to10bit--------------------

%Convert from 16bit to 10bit. Counts are stored in NetCDF as 16bit.
x1 = x1/32; x2 = x2/32; x3 = x3/32; x4 = x4/32; x6 = x6/32;

%--------------------GVARCountToRadiance--------------------

%VISIBLE
%Convert counts to radiance
%Cal coef for GOES-13 imager (average of all 8 detectors for visible)
m = 0.610; b = -17.7; r1 = (m*x1)+b;  % r1 is in W/[m^2-sr-um]

%Convert radiance to reflective
%k coeff for GOES imager.
k = 0.00189544;
R1 = (r1./cSOLZ)*k;
%R1 = (pi*r1)./(1657*cSOLZ);


%INFRARED(RADIATIVE) mW/[m2-sr-cm^-1]
%Atmospheric Absorbtion correction in the IR
```

```
%x2 = x2./cos(SENZ);do not use
%x4 = x4./cos(SENZ);do not use
%x6 = x6./cos(SENZ);do not use

m = 227.3889; b = 68.2167; r2 = (x2-b)/m;    %r is in mW/[m^2-sr-cm^-1]
m = 38.8383;  b = 29.1287; r3 = (x3-b)/m;
m = 5.2285;   b = 15.6854; r4 = (x4-b)/m;
m = 5.5297;   b = 16.5892; r6 = (x6-b)/m;


 %--------------------RadianceToTemperature--------------------

%TEMPERATURE
c1 = 0.00001191066; %[mW/(m^2*sr*cm^-4)]
c2 = 1.438833; %(K/cm^-1)

calib = 1; %1 is 2nd order calibration method
if calib == 0
v = 2561.74; alpha = -1.437204; beta = 1.002562;
T2eff = (c2*v)./log(1+(c1*v^3)./r2); T2 = real(alpha+(beta*T2eff));
v = 1522.52; alpha = -3.625663; beta = 1.010018;
T3eff = (c2*v)./log(1+(c1*v^3)./r3); T3 = real(alpha+(beta*T3eff));
v = 937.23; alpha = -0.386043; beta = 1.001298;
T4eff = (c2*v)./log(1+(c1*v^3)./r4); T4 = real(alpha+(beta*T4eff));
v = 749.83; alpha = -0.134801; beta = 1.000482;
T6eff = (c2*v)./log(1+(c1*v^3)./r6); T6 = real(alpha+(beta*T6eff));
end

if calib == 1
v = 2561.7421; alpha = -1.4755462; beta = 1.0028656; gamma = -0.00000058203946;
T2eff = (c2*v)./log(1+(c1*v^3)./r2); T2 = alpha+(beta*T2eff) + (gamma*T2eff.^2);
v = 1522.5182; alpha = -4.1556932; beta = 1.0142082; gamma = -0.0000080255086;
T3eff = (c2*v)./log(1+(c1*v^3)./r3); T3 = alpha+(beta*T3eff) + (gamma*T3eff.^2);
v = 937.23449; alpha = -0.52227011; beta = 1.0023802; gamma = -0.0000020798856;
T4eff = (c2*v)./log(1+(c1*v^3)./r4); T4 = alpha+(beta*T4eff) + (gamma*T4eff.^2);
v = 749.82589; alpha = -0.16089410; beta = 1.0006896; gamma = -0.00000039853774;
T6eff = (c2*v)./log(1+(c1*v^3)./r6); T6 = alpha+(beta*T6eff) + (gamma*T6eff.^2);
%2nd order
%T2 = alpha+(beta*T2eff) + (gamma*T2eff^2);
 %2/a          2561.7421     -1.4755462=       1.0028656  -5.8203946e-= 07
 %2/b          2561.7421     -1.4755462=       1.0028656  -5.8203946e-= 07
 %3/a          1522.5182     -4.1556932=       1.0142082  -8.0255086e-= 06
 %3/b          1521.6645     -4.1411143=       1.0142255  -8.0755893e-= 06
 %4/a          937.23449     -0.52227011       1.0023802  -2.0798856e-= 06
 %4/b          937.27498     -0.51783545       1.0023789  -2.1027609e-= 06
 %6            749.82589     -0.16089410       1.0006896  -3.9853774e-= 07
%coeff valid between 180 K and 340 K.
end
```

```
%if calib == 2
%v = 2561.74; alpha = -1.437204; beta = 1.002562;
%T2eff = (c2*v)./log(1+(c1*v^3)./r2); T2 = (alpha+(beta*T2eff))./cos(SENZ);
%v = 1522.52; alpha = -3.625663; beta = 1.010018;
%T3eff = (c2*v)./log(1+(c1*v^3)./r3); T3 = (alpha+(beta*T3eff))./cos(SENZ);
%v = 937.23; alpha = -0.386043; beta = 1.001298;
%T4eff = (c2*v)./log(1+(c1*v^3)./r4); T4 = (alpha+(beta*T4eff))./cos(SENZ);
%v = 749.83; alpha = -0.134801; beta = 1.000482;
%T6eff = (c2*v)./log(1+(c1*v^3)./r6); T6 = (alpha+(beta*T6eff))./cos(SENZ);
%end


 %--------------------SWIRtoRefl--------------------

%Since GOES does not include 1.6 band, the refl component of 3.9 will be
%used.
%c1 = 119104200; %(W/m^2*sr*um)
%c2 = 14387.752; %(W/m^2*sr*um^-4)
%v = 3.9; %Wavelength of R2
%alpha = -1.437204; beta = 1.002562; %temp coeff for channel 2
%T = alpha+(beta*T4);
%r2thermal = c1./(v^5*(exp(c2./(v*T))-1)); %Thermal component. Derived from Plank's
function

c1 = 0.00001191066; %[mW/(m^2*sr*cm^-4)]
c2 = 1.438833; %(K/cm^-1)
%alpha = -1.437204; beta = 1.002562; %temp coeff for channel 2
T = alpha+(beta*T4);
v=2561.74;
r2thermal = (c1*v^3)./(exp(c2*(v./T))-1); %Thermal component (mW/[m^2-sr-cm^-1]. Derived
from Plank's function

%fk1=200752;
%fk2=3688.96;
%bc1=1.47950;
%bc2=0.99794;
%cn=2563.9572;
%r2thermal = fk1./(exp(fk2./(bc1+(bc2.*T4)))-1);

r2_corr = (T4-(0.25*(T4-T6))).^4./(T4.^4);
r2thermal = r2thermal.*r2_corr;

toarad = (14.57/pi).*cSOLZ.*exp(-(1-r2_corr)).*exp(-(1-r2_corr).*(cSOLZ./cos(SENZ)));

%toarad = ((14.57/pi)/0.978).*cSOLZ.*exp(-(1-r2_corr)).*exp(-(1-
r2_corr).*(cSOLZ./cos(SENZ)));
R2 = (r2-r2thermal)./(toarad-r2thermal);
```

```
%R2 = ((pi*r2)-r2thermal)./((14.57*cSOLZ) - r2thermal);
R2(R2<0.002)=0.002;
%R2 = r2-r2thermal; %reflective component
%R2 = ((pi*r2)./(14.57*cSOLZ))-r2thermal;
%R2 = (R2./cSOLZ)*100;

%L2(L2<0.01)=0.01;

 %-------------------- Algorithm1--------------------

SST = T4; %(T4 + T6) ./ 2;
SSTf = SST.*(9/5)-459.67;
SSTc = SST.*(1.0)-273.15;
%SST = T4;

SI = R1./R2; %Romanov
%SI = (R1 + R2)./(R1-R2);
%SI(SI<1.01)=1.01;
%SI(SI>1.99)=1.99;
invSI = R2./R1;
%Changing the SST threshold from 273 to 275 for ice and snow increases
%classification near the great lakes in the south.
beginclassification = 1;
if beginclassification == 1

sizeY = dimxlength;
sizeX = dimylength;

Class(sizeX,sizeY)=1;   %1
isLand=zeros(sizeX,sizeY);  %2
isWater=zeros(sizeX,sizeY); %2
isIce=zeros(sizeX,sizeY);   %3
isSnow=zeros(sizeX,sizeY); %4
isCloud=zeros(sizeX,sizeY); %5

%R1Thres = R1threshold(c);
%SIThres = SIthreshold(c);
% R1Thres = 0.09; %0.1;
% R2Thres = 0.05;
% SIThres = 4.5;
 STThres = 271;

 %R1Thres = 0.1; %0.1;
 %R2Thres = 0.05;
 %SIThres = 4.5;
 %STThres = 271;
```

```
Class(R1>=R1Thres & R2 <= R2Thres & SI > SIThres & SST < STThres)=4;
isSnow(Class==4)=1;

Class(R1<R1Thres & R2 < R2Thres & SI <= SIThres & SST < STThres)=3;
isIce(Class==3)=1;

Class(R1<R1Thres & R2 < R2Thres & SI <= SIThres & SST >= STThres)=2;
isWater(Class==2)=1;

Class(isIce~=1 & isWater~=1 & isSnow~=1 & (R1>0.25 | R2>0.1) & SST < STThres)=5;
isCloud(Class==5)=1;

%Class(isIce~=1 & isWater~=1 & isSnow~=1 & isCloud ~= 1 & R1>0.1)=6;
%isLand(Class==6)=1;
end
%Class(isIce~=1 & isWater~=1 & isSnow~=1 & R1>0.1 & R2>0.1 & R2<0.25 & SST > 273 )=6;
%isLand(Class==6)=1;
```